

nature

LOOKING GOOD

An electronic camera shapes up to the human eye

GOOD GENE GUIDE
Secrets of the 'welderly'

DISEASE MODELS
The taming of the mouse

EPIGENOMICS
On the track of drug targets

NATUREJOBS
NIH grant trends

\$10.00US \$12.99CAN



0 71486 03070 6 320

LETTERS

A hemispherical electronic eye camera based on compressible silicon optoelectronics

Heung Cho Ko^{1*}, Mark P. Stoykovich^{1*}, Jizhou Song², Viktor Malyarchuk³, Won Mook Choi¹, Chang-Jae Yu¹, Joseph B. Geddes III⁴, Jianliang Xiao⁷, Shuodao Wang⁷, Yonggang Huang^{7,8} & John A. Rogers^{1,2,3,4,5,6}

The human eye is a remarkable imaging device, with many attractive design features^{1,2}. Prominent among these is a hemispherical detector geometry, similar to that found in many other biological systems, that enables a wide field of view and low aberrations with simple, few-component imaging optics^{3–5}. This type of configuration is extremely difficult to achieve using established optoelectronics technologies, owing to the intrinsically planar nature of the patterning, deposition, etching, materials growth and doping methods that exist for fabricating such systems. Here we report strategies that avoid these limitations, and implement them to yield high-performance, hemispherical electronic eye cameras based on single-crystalline silicon. The approach uses wafer-scale optoelectronics formed in unusual, two-dimensionally compressible configurations and elastomeric transfer elements capable of transforming the planar layouts in which the systems are initially fabricated into hemispherical geometries for their final implementation. In a general sense, these methods, taken together with our theoretical analyses of their associated mechanics, provide practical routes for integrating well-developed planar device technologies onto the surfaces of complex curvilinear objects, suitable for diverse applications that cannot be addressed by conventional means.

The ability to implement electronic and optoelectronic systems on non-planar surfaces could be useful not only for hemispherical cameras and other classes of bio-inspired device designs, but also for conformal integration on or in biological systems as monitoring devices, prosthetics and so on. Unfortunately, existing technologies have been developed only for surfaces of rigid, semiconductor wafers or glass plates and, in more recent work, flat plastic sheets and slabs of rubber. None is suitable for the application contemplated here because the mechanical strains needed to accomplish the planar to hemispherical geometrical transformation (for example up to ~40% for compact eye-type cameras) greatly exceed the fracture strains (for example a few percent) of all known electronic materials, particularly the most well-developed inorganics, even in 'wavy' structural layouts⁶.

One strategy to circumvent these limitations involves adapting all of semiconductor processing and lithography for direct use on curvilinear surfaces. Even a single part of this type of multifaceted procedure—for example lithographic patterning on such surfaces^{7–15} (see also the Ball Semiconductor website, <http://www.ballsemi.com/>) with levels of resolution and multilevel registration that begin to approach those that can be easily achieved on planar surfaces—requires solutions to extremely difficult technical challenges. Although some work based on plastic deformation of planar sheets^{16,17}, self-assembly of small chips^{18,19} and folding of elastic membranes^{20,21} have shown some promise, each has drawbacks and all require certain processing steps to

be performed on a hemispherical or curved surface. Partly as a result, none have been used to achieve the type of cameras contemplated here.

In this paper, we introduce a means of producing curvilinear optoelectronics and electronic eye imagers that uses well-established electronic materials and planar processing approaches to create optoelectronic systems on flat, two dimensional surfaces in unusual designs that tolerate compression and stretching to large levels of strain (~50% or more). Conceptually this feature enables planar layouts to be geometrically transformed (that is conformally wrapped) to nearly arbitrary curvilinear shapes. In the example presented here, we use a hemispherical, elastomeric transfer element to accomplish this transformation with an electrically interconnected array of single-crystalline silicon photodiodes and current-blocking p–n junction diodes assembled in a passive matrix layout. The resulting hemispherical focal plane arrays, when combined with imaging optics and hemispherical housings, yield electronic cameras that have overall sizes and shapes comparable to the human eye. Experimental demonstrations and theoretical analyses reveal the key aspects of the optics and mechanics of these systems.

Figure 1 illustrates the main steps in the fabrication. The process begins with the formation of a hemispherical, elastomeric transfer element by casting and curing a liquid prepolymer to poly(dimethylsiloxane) (PDMS) in the gap between opposing convex and concave lenses with matching radii of curvature (~1 cm). A jig specially designed to hold these lenses also provides a raised rim around the perimeter of the resulting piece of PDMS. This transfer element is mounted into a mechanical fixture that provides coordinated radial motion of ten independent paddle arms that each inserts into the rim. Translating the arms of this radial tensioning stage outwards expands the hemisphere. The associated reversible, elastic deformations in the PDMS transform this hemisphere, at sufficiently large tension, into the planar shape of a 'drumhead', such that all points in the PDMS are in biaxial tension. The extent of expansion and the underlying mechanics determine the overall magnitude of this tension.

Separately, conventional planar processing forms a passive matrix focal plane array on a silicon-on-insulator wafer consisting of single-crystalline silicon photodetectors, current-blocking p–n junction diodes and metal (chromium–gold–chromium) interconnects, with films of polymer (polyimide) to support certain regions and to encapsulate the entire system. A critically important design feature is the use of thin, narrow lines to connect nearest-neighbour pixel elements; these structures enable elastic compressibility in the system, as described below. Removing the buried oxide layer of the silicon-on-insulator wafer by etching with concentrated hydrofluoric acid in a manner that leaves the focal plane array supported by polymer posts

¹Department of Materials Science and Engineering, ²Department of Mechanical Science and Engineering, ³Frederick-Seitz Materials Research Laboratory, ⁴Beckman Institute for Advanced Science and Technology, ⁵Department of Electrical and Computer Engineering, ⁶Department of Chemistry, University of Illinois at Urbana-Champaign, Urbana, Illinois 61801, USA. ⁷Department of Mechanical Engineering, ⁸Department of Civil and Environmental Engineering, Northwestern University, Evanston, Illinois 60208, USA.

*These authors contributed equally to this work.

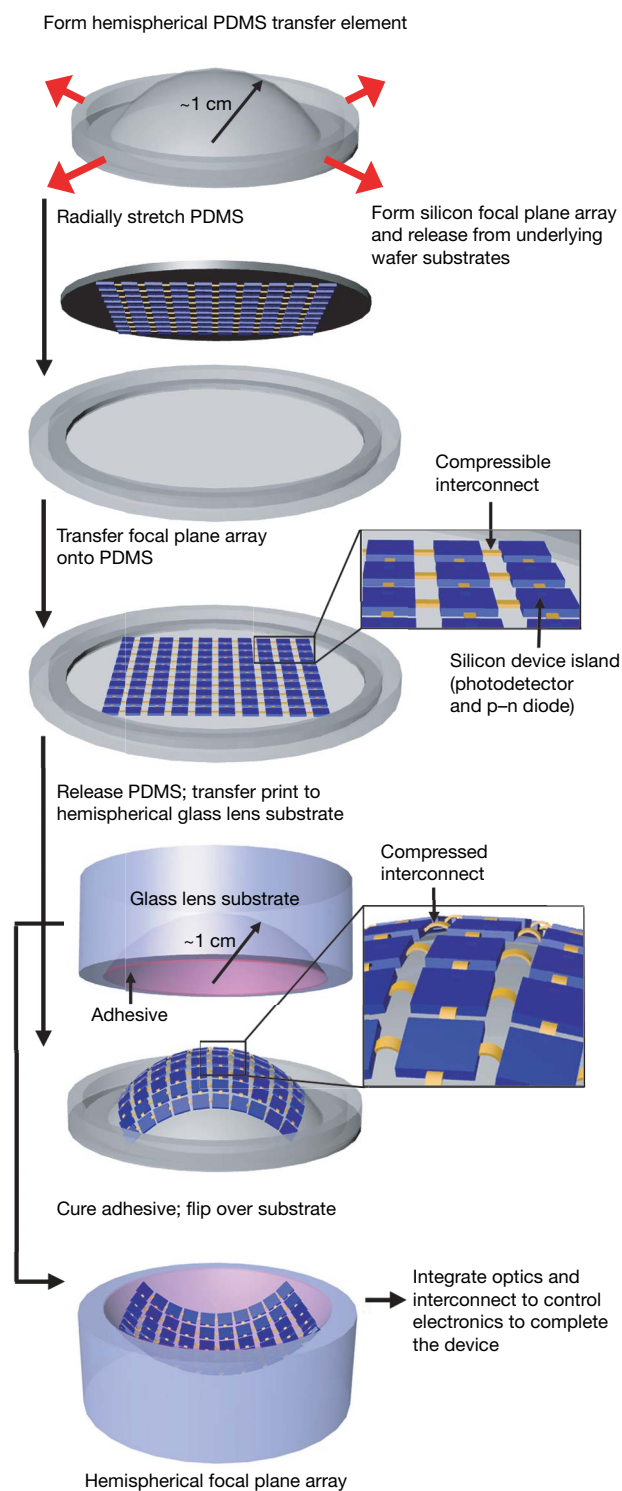


Figure 1 | Illustration of steps for using compressible silicon focal plane arrays and hemispherical, elastomeric transfer elements to fabricate electronic eye cameras. The top frame shows such a transfer element, fabricated in PDMS by casting and curing against an appropriately designed template. Stretching in the radial direction forms a flat drumhead membrane in which all points in the PDMS are in tension. Lifting a prefabricated focal plane array and associated electronics from a source wafer onto the surface of this drumhead, and then allowing the PDMS to relax back to its initial shape, transforms the planar device layout into a hemispherical shape. Transfer printing onto a matching hemispherical glass substrate coated with a thin layer of a photocurable adhesive (pink), adding a hemispherical cap with integrated imaging lens and interfacing to external control electronics (not shown here) completes the camera system.

but otherwise raised above the underlying silicon ‘handle’ wafer completes the device processing. Fabrication of the interconnected pixel arrays on rigid, planar substrates using established processing techniques avoids limitations, for example in registration, that are often encountered in soft electronics. (Fabrication details appear in the Supplementary Information.)

Bringing the transfer element in its tensioned, planar drumhead shape into contact with this wafer and then peeling it away lifts up the focal plane array, leaving it stuck to the soft surface of the elastomer through non-specific van der Waals interactions^{22,23}. Moving the paddle arms of the tensioning stage inwards to their initial positions causes the elastomer to relax back, approximately, to its initial hemispherical shape but with a slightly ($\sim 10\%$ for the systems investigated here) larger radius of curvature. In this process, compressive forces act on the focal plane array to bring the pixel elements closer together, with magnitudes that correspond to significant compressive strains (up to 10–20%, depending on the applied tension). The narrow, thin connecting lines accommodate these large strains by delaminating locally from the surface of the elastomer to adopt arc shapes pinned on the ends by the detector pixels (that is, the pixels are not substantially deformed and the interconnect strains are up to ~ 20 –40%), with a mechanics conceptually similar to related responses in stretchable semiconductor ribbons²⁴. This process allows the planar-to-spherical geometrical transformation to be accomplished without creating substantial strains in any of the active components of the focal plane array. The hemispherical, elastomeric transfer element, ‘inked’ with the focal plane array in this manner, enables transfer ‘printing’ onto a hemispherical glass substrate that has a matching radius of curvature and is coated with a thin layer of a photocurable adhesive. Mounting the resulting system on a printed circuit board with bus lines to external control electronics, establishing electrical connections to pinouts located along the perimeter of the detector array, and integrating with a hemispherical cap fitted with a simple imaging lens completes the hemispherical electronic eye camera. (Details appear in the Supplementary Information.)

The fabrication approach summarized in Fig. 1 can be applied to planar electronics and optoelectronics technologies with nearly arbitrary materials classes and devices, provided that they incorporate appropriately configured compressible interconnects. A key advantage of the strategy is that the most labour-intensive part of the process, that is, formation of the pixel arrays themselves, is fully compatible with the capabilities of existing, planar silicon device manufacturing facilities. Figure 2 outlines the designs and processes implemented in constructing the hemispherical cameras described here. Each pixel in the 16-by-16 imaging array supports two devices—a photodetecting diode and a p–n junction blocking diode—monolithically formed in a single piece of single-crystalline silicon ($500 \times 500 \mu\text{m}^2$ in area, $1.2 \mu\text{m}$ thick) with a capping layer of polyimide ($560 \times 560 \mu\text{m}^2$ in area, 1 – $1.5 \mu\text{m}$ thick): the first device provides local light detection; the second enables current blocking and enhanced isolation for passive matrix readout. Layers of metal above each of the blocking diodes shield them from light, thereby removing their photoresponses. The layout of these layers, the two devices and the electrical connections are illustrated in the schematic view and optical image in Fig. 2a. The pixel-to-pixel interconnects consist of thin layers of patterned metal ($360 \mu\text{m}$ long, $50 \mu\text{m}$ wide, $3:150:3 \text{ nm}$ thick (chromium:gold:chromium)) on thin layers of polyimide ($360 \mu\text{m}$ long, $110 \mu\text{m}$ wide, 1 – $1.5 \mu\text{m}$ thick), spin-cast and patterned in conventional ways.

The images in Fig. 2b, c shows a 16-by-16 array of photodetecting diode–blocking diode pixels transferred onto the surface of a hemispherical, elastomeric transfer element, corresponding to the next-to-last diagram in Fig. 1. The arc-shaped interconnections that enable the planar to hemispherical transformation can be seen clearly. The yields associated with the transfer process and the formation of these types of stretchable connections are high; 100% of the pixels and interconnections in the case of the 16-by-16 arrays have been

reproducibly transferred. Greater than 95% yields have also been demonstrated for the transfer of higher density arrays of passive silicon elements ($20 \times 20 \mu\text{m}^2$ in area, 50 nm thick) and nearest-neighbour connections ($20 \mu\text{m}$ long, $4 \mu\text{m}$ wide, 50 nm thick) (see Supplementary Fig. 9).

Significant mechanical deformations in the imaging arrays are generated during the transfer process, specifically during the planar to hemispherical transformation of the elastomeric transfer element. Simple mechanics models, based on plate theory and confirmed using established finite element analysis techniques, have been developed to determine the spatial distributions of pixels during the transfer process, as well as the distributions of stresses and

displacements in the interconnections and silicon pixels (see Supplementary Information). These models indicate that the imaging arrays on the hemispherical surface have very small variations ($\sim 3\%$ maximum to minimum) in the local pitch and a relatively uniform pitch $\sim 10\%$ smaller than the arrays in the planar, as-fabricated geometry. In addition, the mechanics models predict maximum strains of $\sim 0.01\%$ in the silicon pixels and $\sim 0.3\%$ in the metal of the arc-shaped interconnects for the $\sim 20\%$ change in interconnection length ($\sim 10\%$ change in pitch) observed in these systems. Figure 2d is an image of a completed array on a hemispherical glass substrate, corresponding to the last frame in Fig. 1. The high level of engineering control over the fabrication process is evident from the uniformity of the structures that can be transferred to the hemispherical substrate.

Figure 2e shows the current–voltage response of a representative individual pixel in a hemispherical detector array (black, shielded from light; red, exposed to light), addressed by means of row and column electrodes through contact pads at the perimeter of the 16-by-16 array. Similar responses are achieved for individual pixels in planar imaging arrays (see Supplementary Fig. 15). Key features are the strong photoresponse (main frame), the very low reverse bias current (inset), and low crosstalk (inset) between pixels in passive matrix addressing. (Additional details of the device layouts, the electrical properties and the mechanics analysis appear in the Supplementary Information.)

Electrical connections from the row and column contacts at the periphery of the passive matrix array are made to pre-patterned lines on a printed circuit board. The resulting system (Fig. 3a) is interfaced with a computer with specially designed software for acquiring images from the camera. The external electrical connections are formed by evaporating metal over the edge of the concave glass substrate through a flexible shadow mask. Currently, the electrode lines that connect the periphery of the pixel arrays to separate control electronics limit yields and set practical bounds on pixel counts. With unoptimized manual systems, the interconnects from the periphery of the pixel array to the printed circuit board can be registered to an accuracy of $\pm 200 \mu\text{m}$. Integration with a hemispherical cap fitted with a simple, single-element lens that provides the imaging optics completes the camera, as illustrated in Fig. 3b, c.

Figure 3d shows images collected with the hemispherical electronic eye camera of Fig. 3a–c. The optical setup for these results used collimated green light (argon ion laser) to illuminate a printed pattern on a transparency film. The transmitted light passed through a simple plano-convex lens (diameter, 25.4 mm; focal length, 35 mm) to form an image on the hemispherical camera (see Supplementary Information and Supplementary Fig. 16). The left-hand frame of Fig. 3d shows the direct output of the camera for the case of an image

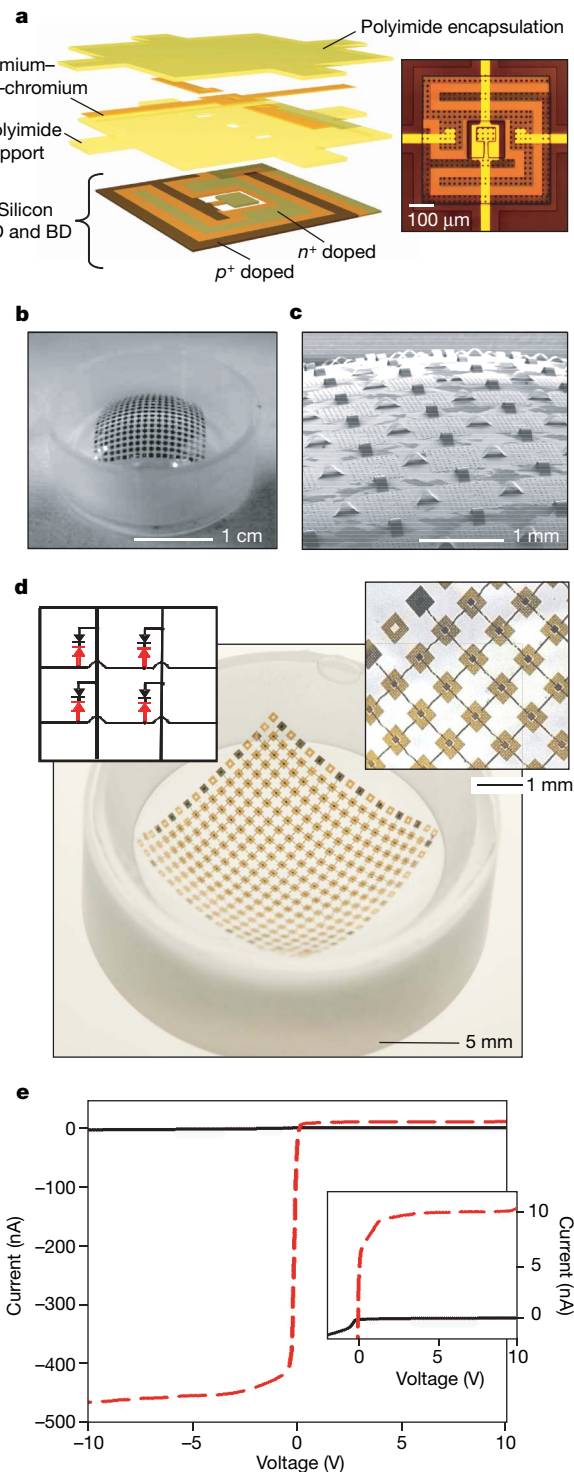


Figure 2 | Design and electrical properties of a hemispherical electronic eye camera based on single-crystalline silicon photodetectors and current-blocking p–n junction diodes in a compressible, passive matrix layout.

a, Exploded schematic of the layout of the silicon, metal and polymer associated with a single unit cell in the array. The blocking diode (BD) is in the centre of the cell; the photodetector (PD) is in a serpentine geometry around the BD. **b**, Photograph of a hemispherical PDMS transfer element with a compressible focal plane array on its surface. **c**, Scanning electron microscope image of a portion of the array in **b**, illustrating the compressible interconnects. **d**, Photograph of the array integrated on a hemispherical glass substrate (main frame), optical micrograph of a part of the array (upper right inset) and circuit diagram showing the BDs (black), PDs (red) and electrode crossovers (arcs) in a 2-by-2 section of the system (upper left inset). **e**, Electrical properties of a unit cell. The data were measured by contacting the row and column electrodes that address this position in the hemispherical array, by means of pads at the perimeter of the system. The data (black, shielded from light; red, exposed to light) show a high-contrast response to light exposure. Equally importantly, the reverse bias current and leakage from other pixels in the array are both minimal, as shown in the inset.

of the top two rows of the standard eye chart²⁵. Although the shapes of the letters are clearly resolved, the fine spatial features of the smaller text are not accurately represented, owing to the relatively low numbers of pixels in these cameras. The image quality can be improved by implementing a strategy adapted from biological systems, in which a sequence of images is collected as the camera is eucentrically rotated in the θ and φ directions (θ , azimuthal angle in the plane normal to the optical axis; φ , polar angle measured from the optical axis) relative to the object. Reconstruction, using pixel positions on the hemispherical surface predicted with mechanics models described in the Supplementary Information, yields high-resolution images. The right-hand frame of Fig. 3d is a picture acquired by rapidly scanning a small range of angles (from -2° to 2° in both θ and φ) in 0.4° increments.

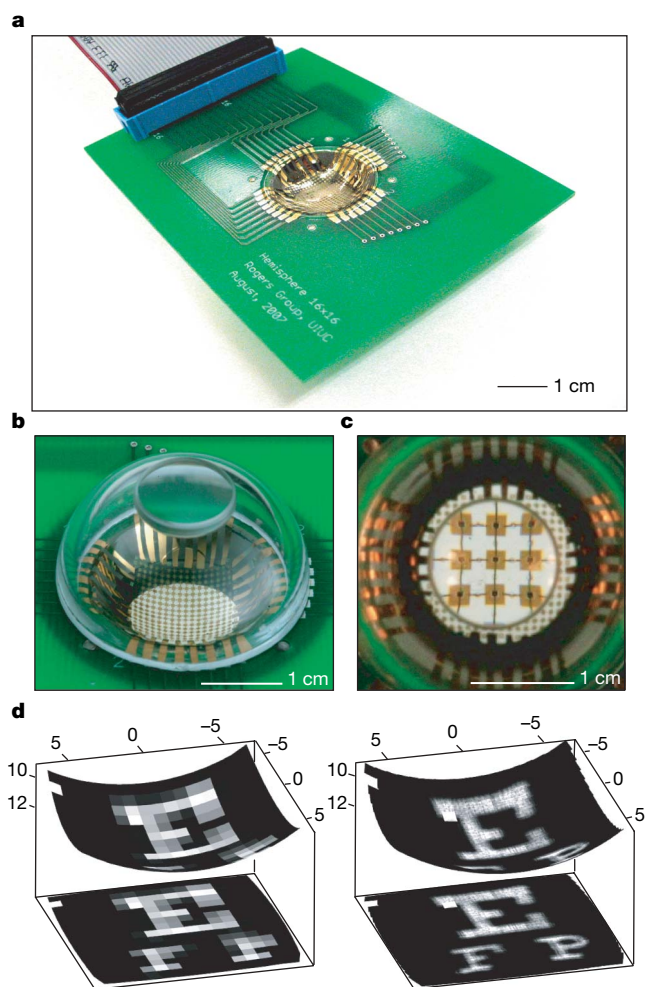


Figure 3 | Photographs of a hemispherical electronic eye camera and representative output images. **a**, Photograph of a hemispherical focal plane array (centre) mounted on a printed circuit board (green), with external connection to a computer (not shown) through a ribbon cable (upper left). **b**, Photograph of the camera after integration with a transparent (for ease of viewing) hemispherical cap with a simple, single-component imaging lens (top). **c**, Close-up photograph of the system in **b**, as viewed directly through the imaging lens. For the parameters used here, this lens magnifies the focal plane array to show a small, 3-by-3 cluster of pixels. **d**, Greyscale images of the first two rows in an eye chart acquired using a hemispherical camera with a 16-by-16 pixel array, as displayed on a hemispherical surface matching the detector surface (top) and projected onto a plane (bottom). The images on the left and right were acquired without scanning and with scanning (from -2° to 2° in the θ and φ directions, in 0.4° increments), respectively. The axis scales are in millimetres and are identical in each image.

Even more complex pictures (Fig. 4a, b) can be obtained at high resolution using this simple scanning approach (-2° to 2° in both θ and φ , 0.4° increments). Inspection of the images suggests that the stitching errors associated with this process are $<40\ \mu\text{m}$, thereby validating the accuracy of these models. The nearest-neighbour pixels in the hemispherical camera are separated by $\sim 4^\circ$, leading to zero redundancy in generating the tiled picture. These results also demonstrate the high yield of functional pixels, namely $>99\%$ (254 out of 256). Supplementary Figs 18 and 19 show images acquired from each

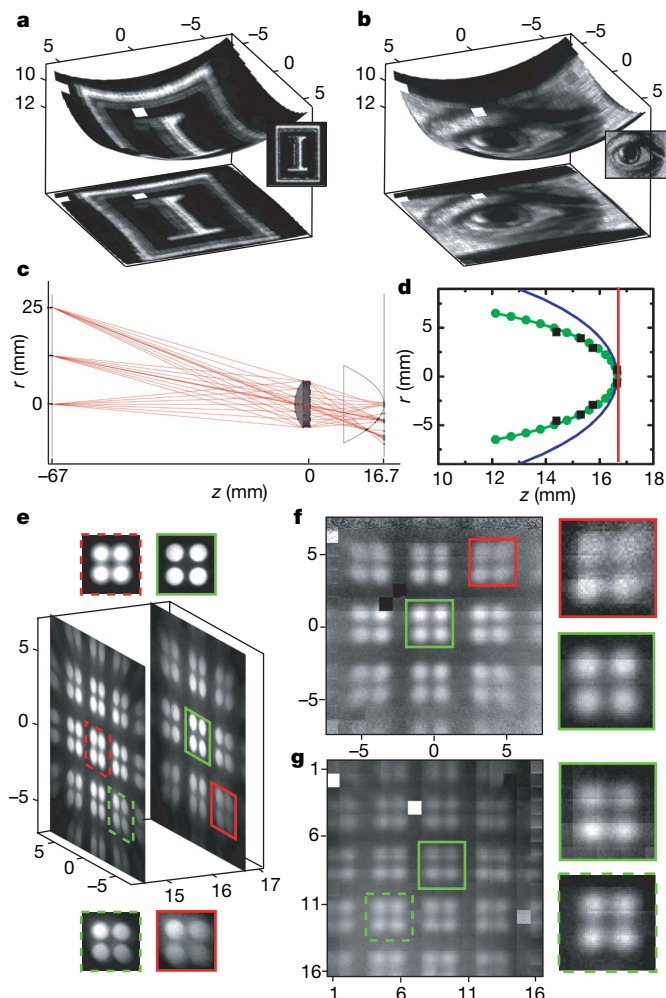


Figure 4 | Enhanced imaging in hemispherical cameras in comparison with planar cameras. High-resolution images of the University of Illinois 'I' logo (**a**) and a drawing of an eye acquired with a hemispherical camera (**b**; insets on the right of **a** and **b** show the original images scanned from the transparency films). **c**, Optics set-up used for imaging and sample ray traces showing a pattern of rays passing through the image and lens onto the detector screens (optimal focal surface and planar camera). Plotted using the Rayica 3.0 package, Optica Software, Champaign, Illinois, USA. **d**, Ray tracing predictions of the curvature of the optimal focal surface (green circles, calculated focal points; green curve, parabolic fit), the detector surface of the hemispherical camera (blue curve), and a planar camera (red curve). **e**, High-resolution photographs of projected images on a planar screen positioned at varying distances from the lens. The left- and right-hand images were acquired at distances $z = 14.40\ \text{mm}$ and $z = 16.65\ \text{mm}$ from the lens, respectively, and demonstrate a shift in optimal focus as a function of detector position. A series of such images was used to estimate the optimal curvilinear focal surface, shown in **d** as black squares. **f**, **g**, High-resolution images acquired with planar (**f**) and hemispherical (**g**) cameras positioned $16.65\ \text{mm}$ from the lens (along the optical axis). All axis scales are in millimetres except for those in **g**, in which pixel number is plotted, and the axes normal to the image planes represent the z direction (optical axis).

pixel when scanned over the entire projected image (from -40° to 40° in both θ and ϕ), further demonstrating the high quality and uniformity of the pixels in the array.

The simple, single-lens system considered here provides a clear example of how curved detectors can improve camera performance. The focusing ability of hemispherical and planar cameras is compared in Fig. 4c–g using fabricated devices, ray tracing software and commercial cameras. An ideal imaging system would perfectly reproduce the image on the detector surface; however, the lens introduces aberrations that degrade the image quality. Complex and expensive optics can reduce the third-order Seidel aberrations for planar detector surfaces, but such aberrations play a significant role in the focusing ability of the simple, single-lens arrangements of interest here^{3,26}. A demonstration of focusing abilities requires non-collimated light sources and a wide aperture for a large field of view; thus, the optical test set-up for Fig. 4c–g uses rear-illumination of a pattern printed on paper with halogen lamps and a high-numerical-aperture plano-convex lens (diameter, 12 mm; focal length, 12 mm). Use of optical filters to limit the incident-light wavelength to ~ 620 – 700 nm minimizes contributions from chromatic aberrations.

Figure 4c shows the optics arrangement and representative ray traces used to calculate the curvilinear image surface (see Supplementary Information). The calculated surface corresponds, to a good approximation, to a paraboloid of revolution (see Fig. 4d) and is much closer in shape to the hemispherical detector than the planar detector. Figure 4e shows images projected on a planar screen (photographic plastic film) obtained with a commercial camera at two different distances z (left, $z = 14.40$ mm; right, $z = 16.65$ mm) between the screen and lens along the optical axis. The position of best focus shifts from the centre to the edge of the image with decreasing z . The image surface estimated using a series of such photographs is similar to that predicted by the ray tracing theory (see Fig. 4d and Supplementary Figure 20). Figure 4f, g compares images acquired with the fabricated planar and hemispherical cameras, respectively. The hemispherical system has a number of advantages, including more uniform focus from the centre to the edge, a wider field of view, more homogeneous intensity throughout the image and reduced geometric distortions. Many of these features are evident in Fig. 4f, g even at the modest levels of resolution associated with these particular devices.

In conclusion, we note that the compressible optoelectronics and elastomeric transfer element strategies introduced here are compatible with high-resolution focal plane arrays, other more advanced materials systems and device designs, and refined substrate shapes (for example parabolic or other aspherical surfaces). Demonstrating these possibilities, exploring applications in other areas, and defining the fundamental limits associated with the materials, layouts and mechanics of the compressible interconnects represent promising topics for future work.

METHODS SUMMARY

Fabrication of hemispherical cameras. A hemispherical, elastomeric transfer element was molded in poly(dimethylsiloxane) (Sylgard 184, Dow Corning) by curing a liquid prepolymer between convex and concave lenses with identical radii of curvature (12.9 mm, CVI Laser Optics). Coordinated radial stretching of the transfer element such that the hemispherical surface could be reversibly deformed to a planar drumhead surface was performed using a custom-designed mechanical stage. A passive matrix focal plane array was fabricated separately on a planar silicon-on-insulator wafer (1.2- μm -thick silicon layer on a 400-nm-thick silicon dioxide insulator layer, Soitec) using conventional semiconductor processing. The buried oxide layer in the silicon-on-insulator wafer was removed after complete fabrication of the detector array by etching with concentrated hydrofluoric acid and this wafer was contacted to the radially tensioned transfer element in its planar drumhead shape. The focal plane array was lifted onto this planar elastomeric transfer element after peeling away the wafer and remained adhered through intermolecular van der Waals interactions. Relaxing the tension on the planar elastomeric transfer element transformed the focal plane array and transfer element into approximately the original hemispherical surface. The focal plane array was then transfer printed from the hemispherical transfer

element onto a matching concave glass substrate coated with a thin layer of photocurable adhesive (NOA 73, Norland). The hemispherical substrate was mounted in a printed computer board and electrical connections to external pinouts were made from metal evaporated through an elastomeric shadow mask.

Imaging with hemispherical cameras. The hemispherical cameras collected images using two distinct set-ups. Collimated laser light (argon ion laser; Figs 3d and 4a, b) and non-collimated light sources (halogen lamps; Figs 4e–g) illuminated a pattern printed on transparency and paper screens, respectively. The transmitted light then passed through a single plano-convex lens to form an image on the hemispherical camera.

Received 1 February; accepted 20 May 2008.

- Land, M. F. & Nilsson, D.-E. *Animal Eyes* (Oxford Univ. Press, New York, 2002).
- Goldsmith, T. H. Optimization, constraint, and history in the evolution of eyes. *Q. Rev. Biol.* **65**, 281–322 (1990).
- Walther, A. *The Ray and Wave Theory of Lenses* (Cambridge Univ. Press, Cambridge, UK, 1995).
- Swain, P. & Mark, D. Curved CCD detector devices and arrays for multi-spectral astrophysical applications and terrestrial stereo panoramic cameras. *Proc. SPIE* **5499**, 281–301 (2004).
- Grayson, T. Curved focal plane wide field of view telescope design. *Proc. SPIE* **4849**, 269–274 (2002).
- Khang, D. Y., Jiang, H., Huang, Y. & Rogers, J. A. A stretchable form of single crystal silicon for high performance electronics on rubber substrates. *Science* **311**, 208–212 (2006).
- Jackman, R. J., Wilbur, J. L. & Whitesides, G. M. Fabrication of submicrometer features on curved substrates by microcontact printing. *Science* **269**, 664–666 (1995).
- Paul, K. E., Prentiss, M. & Whitesides, G. M. Patterning spherical surfaces at the two-hundred nanometer scale using soft lithography. *Adv. Funct. Mater.* **13**, 259–263 (2003).
- Miller, S. M., Troian, S. M. & Wagner, S. Direct printing of polymer microstructures on flat and spherical surfaces using a letterpress technique. *J. Vac. Sci. Technol. B* **20**, 2320–2327 (2002).
- Childs, W. R. & Nuzzo, R. G. Patterning of thin-film microstructures on non-planar substrate surfaces using decal transfer lithography. *Adv. Mater.* **16**, 1323–1327 (2004).
- Lee, K. J., Fosser, K. A. & Nuzzo, R. G. Fabrication of stable metallic patterns embedded in poly(dimethylsiloxane) and model applications in non-planar electronic and lab-on-a-chip device patterning. *Adv. Funct. Mater.* **15**, 557–566 (2005).
- Lima, O., Tan, L., Goel, A. & Negahban, M. Creating micro- and nanostructures on tubular and spherical surfaces. *J. Vac. Sci. Technol. B* **25**, 2412–2418 (2007).
- Radtke, D. & Zeitner, U. D. Laser-lithography on non-planar surfaces. *Opt. Express* **15**, 1167–1174 (2007).
- Rucheheft, P. & Wolfe, J. C. Optimal strategy for controlling linewidth on spherical focal surface arrays. *J. Vac. Sci. Technol. B* **18**, 3185–3189 (2000).
- Xia, Y. *et al.* Complex optical surfaces formed by replica molding against elastomeric masters. *Science* **273**, 347–349 (1996).
- Hsu, P. I. *et al.* Spherical deformation of compliant substrates with semiconductor device islands. *J. Appl. Phys.* **95**, 705–712 (2004).
- Hsu, P. I. *et al.* Effects of mechanical strain on TFTs on spherical domes. *IEEE Trans. Electron. Dev.* **51**, 371–377 (2004).
- Jacobs, H. O., Tao, A. R., Schwartz, A., Gracias, D. H. & Whitesides, G. M. Fabrication of a cylindrical display by patterned assembly. *Science* **296**, 323–325 (2002).
- Zheng, W., Buhlmann, P. & Jacobs, H. O. Sequential shape-and-solder-directed self-assembly of functional microsystems. *Proc. Natl Acad. Sci. USA* **101**, 12814–12817 (2004).
- Boncheva, M. *et al.* Magnetic self-assembly of three-dimensional surfaces from planar sheets. *Proc. Natl Acad. Sci. USA* **102**, 3924–3929 (2005).
- Boncheva, M. & Whitesides, G. M. Templated self-assembly: Formation of folded structures by relaxation of pre-stressed, planar tapes. The path to ubiquitous and low-cost organic electronic appliances on plastic. *Adv. Mater.* **17**, 553–557 (2005).
- Huang, Y. Y. *et al.* Stamp collapse in soft lithography. *Langmuir* **21**, 8058–8068 (2005).
- Zhou, W. *et al.* Mechanism for stamp collapse in soft lithography. *Appl. Phys. Lett.* **87**, 251925 (2005).
- Sun, Y. *et al.* Controlled buckling of semiconductor nanoribbons for stretchable electronics. *Nature Nanotechnol.* **1**, 201–207 (2006).
- Begbie, G. H. *Seeing and the Eye* 92–93 (Natural History Press, Garden City, New York, 1969).
- Born, M. & Wolf, E. *Principles of Optics* 7th edn (Cambridge Univ. Press, New York, 1999).

Supplementary Information is linked to the online version of the paper at www.nature.com/nature.

Acknowledgements We thank T. Banks, K. Colravy, and J. A. N. T. Soares for help using facilities at the Frederick Seitz Materials Research Laboratory. The materials and optics aspects were developed in work supported by the US Department of Energy, Division of Materials Sciences under Award No. DE-FG02-07ER46471,

through the Materials Research Laboratory and Center for Microanalysis of Materials (DE-FG02-07ER46453) at the University of Illinois at Urbana-Champaign. The processing approaches and the mechanics were developed in work supported by the National Science Foundation under grant DMI-0328162. C.-J.Y. acknowledges financial support from the Korea Research Foundation (grant KRF-2005-214-D00329) funded by the Korean Government (MOEHRD). J.B.G. acknowledges support from a Beckman postdoctoral fellowship.

Author Contributions H.C.K., M.P.S., V.M. and J.A.R. designed the experiments. H.C.K., M.P.S., J.S., V.M., W.M.C, C.-J.Y., J.B.G., J.X., S.W., Y.H. and J.A.R. performed the experiments and analysis. H.C.K., M.P.S., J.S., Y.H. and J.A.R. wrote the paper.

Author Information Reprints and permissions information is available at www.nature.com/reprints. Correspondence and requests for materials should be addressed to J.A.R. (jrogers@uiuc.edu) and Y.H. (y-huang@northwestern.edu).

A hemispherical electronic eye camera based on compressible silicon optoelectronics (Supplementary Information)

Heung Cho Ko^{1*}, Mark P. Stoykovich^{1*}, Jizhou Song², Viktor Malyarchuk³, Won Mook Choi¹, Chang-Jae Yu¹, Joseph B. Geddes III⁴, Jianliang Xiao⁵, Shuodao Wang⁵, Yonggang Huang^{5,6} and John A. Rogers^{1-4,7,8}

¹*Department of Materials Science and Engineering*, ²*Department of Mechanical Science and Engineering*, ³*Frederick-Seitz Materials Research Laboratory*, ⁴*Beckman Institute for Advanced Science and Technology*, ⁷*Department of Electrical and Computer Engineering*, ⁸*Department of Chemistry, University of Illinois at Urban-Champaign, Urbana, Illinois 61801, USA*

⁵*Department of Mechanical Engineering*, ⁶*Department of Civil and Environmental Engineering*, *Northwestern University, Evanston, IL 60208*

*These authors contributed equally to this work.

This PDF file includes Supplementary Methods and Discussion; Supplementary Figures and Legends S1-S29.

Table of Contents

Supplementary Methods and Discussion	Page
Planar Processing of the Focal Plane Array	S3
Fabricating the Hemispherical PDMS Transfer Element	S6
Stretching the PDMS Transfer Element and Transfer Printing	S6
Integrating with Hemispherical Cap and Imaging Lens	S7
Imaging with the Camera	S7
Comparison of aberrations in hemispherical and planar detectors: Experiments	S9
Comparison of aberrations in hemispherical and planar detectors: Theory	S10
Mapping of Silicon Elements onto a Hemisphere	S11
Arc-Shaped Connections between Silicon Elements	S13
Strain Distributions in Silicon Elements	S13
References	S14
Supplementary Figures and Legends S1 – S29	S15-S43

Supplementary Methods and Discussion

Nearly all of the materials and methods relied on specialized setups specifically designed for this project, including certain of the planar processing steps and circuit liftoff strategies, the compressible interconnect layouts, the hemispherical PDMS transfer elements, the radial tensioning stages, the fixtures and lens systems, the mux/demux interfaces and the computer software control. The following describes the essential features of these systems.

Planar Processing of the Focal Plane Array:

The sequence of processing steps used to form the focal plane arrays appears below. A key part of the fabrication is the formation of polymer posts that support the array during undercut etching of the buried oxide (steps 34-37). Figure S1 highlights this processing. Figure S2 schematically illustrates the layout of the array, and provides key dimensions. Figure S3 presents images of a complete array and micrographs of features of the unit cell, for the simple system of a planar camera with designs that are otherwise similar to those used for the hemispherical system.

– Processing Scheme for Focal Plane Arrays on SOI –

Pattern alignment marks

1. Clean a 1.2 μm SOI wafer chip (Soitec) (acetone, IPA, water \rightarrow drying 5 min at 110 $^{\circ}\text{C}$).
2. HMDS pretreatment for 1.5 min.
3. Pattern photoresist (PR; Clariant AZ5214, 3000 rpm, 30s) with 365 nm optical lithography through chrome mask (Karl Suss MJB3).
Develop in aqueous base developer (MIF 327).
4. Reactive ion etch (RIE; PlasmaTherm 790 Series, 50 mTorr, 40 sccm SF_6 , 100 W, 20 s).
5. Remove PR. Acetone rinse and then piranha treatment ($\sim 3:1 \text{ H}_2\text{SO}_4:\text{H}_2\text{O}_2$ for 1 min).

p⁺ doping

6. HF cleaning (Fisher, concentrated 49%, 2 sec).
7. Plasma enhanced chemical vapor deposition (PECVD; PlasmaTherm SLR) of 600 nm SiO_2 .
8. HMDS 1.5 min.
9. Pattern PR.
10. Anneal 5 min.
11. Etch oxide with buffered oxide etch (BOE, 2 min).
12. Remove PR. Acetone rinse and then piranha treatment for 3 min.

13. BOE for 2s.
14. Anneal at 200°C for 10 min.
15. Spin-on-dopant (p-type, Boron, Filmtronics B219, 3000 rpm, 30 s).
16. Anneal at 200°C for 10 min.
17. Anneal at 1050°C for 30 min in 4:1 N₂:O₂.
18. Cleaning (HF for 30 s, 1:1 HNO₃:H₂SO₄ for 5 min, BOE for 1 min).

n⁺ doping

19. PECVD 600 nm SiO₂.
20. HMDS 1.5 min.
21. Pattern PR.
22. Anneal 5 min.
23. Etch oxide with buffered oxide etch (BOE, 2 min).
24. Remove PR. Acetone rinse and then piranha treatment for 3 min.
25. BOE for 2s.
26. Anneal at 200°C for 10 min.
27. Spin-on-dopant (n-type, Phosphorous, Filmtronics P506, 3000 rpm, 30 s).
28. Anneal at 200°C for 10 min.
29. Anneal at 950°C for 20 min in 4:1 N₂:O₂.
30. Cleaning (BOE for 4 min, piranha for 3 min, BOE for 1 min).

Define PD and BD structures

31. Pattern PR.
32. RIE (50 mTorr, 40 sccm SF₆, 100 W, 4 min).
33. Remove PR. Acetone rinse and then piranha treatment for 3 min.

Pre-treatment with sacrificial oxide layer

34. HF for 90 s.
35. PECVD 100 SiO₂.
36. Pattern PR.
37. BOE for 30 s.
38. Remove PR. Acetone rinse and then piranha treatment for 3 min.

Deposit and pattern PI support layer

39. Spin coat with polyimide (PI, poly(pyromellitic dianhydride-co-4,4'-oxydianiline), amic acid solution, Sigma-Aldrich, spun at 4,000 rpm for 60 s).
40. Anneal at 110°C for 3 min and 150°C for 10 min.
41. Anneal at 250°C for 2 h in N₂ atmosphere.
42. Ultraviolet ozone (UVO) treatment for 5 min.
43. PECVD 200 nm SiO₂.
44. HMDS 1.5 min.
45. Pattern PR.
46. RIE (50 mTorr, 40:1.2 sccm CF₄:O₂, 150 W, 10 min).
47. Remove PR. Acetone rinse.
48. RIE (50 mTorr, 20 sccm O₂, 150 W, 13 min).

Deposit and pattern metal layer

49. BOE for 40 s.

50. Sputter 3/150/3 nm of Cr/Au/Cr.
51. PECVD 200 nm SiO₂.
52. HMDS 1.5 min.
53. Pattern PR.
54. RIE (50 mTorr, 40:1.2 sccm CF₄:O₂, 150 W, 10 min).
55. Wet etch Cr/Au/Cr for 20/40/20s (Transene etchants).
56. Remove PR. Acetone rinse.
57. Remove SiO₂. BOE for 60 s.

Deposit PI and pattern holes for oxide box layer etch

58. Spin coat with PI.
59. Anneal at 110°C for 3 min, at 150°C for 10 min.
60. Anneal at 250°C for 2 h in N₂ atmosphere.
61. UVO treatment for 5 min.
62. PECVD 200 nm SiO₂.
63. HMDS 1.5 min.
64. Pattern PR.
65. RIE (50 mTorr, 40:1.2 sccm CF₄:O₂, 150 W, 10 min).
66. Remove PR. Acetone rinse.
67. RIE (50 mTorr, 20 sccm O₂, 150 W, 10 min).
68. Wet etch Cr/Au/Cr for 8/20/8 s.
69. RIE (50 mTorr, 20 sccm O₂, 150 W, 13 min).
70. RIE (50 mTorr, 40 sccm SF₆, 100 W, 5.5 min).

PI isolation

71. BOE for 40 s.
72. UVO treatment for 5 min
73. PECVD 200 nm SiO₂.
74. HMDS 1.5 min.
75. Pattern PR.
76. RIE (50 mTorr, 40:1.2 sccm CF₄:O₂, 150 W, 10 min).
77. Remove PR. Acetone rinse.
78. RIE (50 mTorr, 20 sccm O₂, 150 W, 16 min).

Box etching and transfer

79. HF for 30 min to etch oxide box layer and release array from handle wafer.
80. Transfer and printing processes.

Fabricating the Hemispherical PDMS Transfer Element:

Casting and curing procedures formed these transfer elements out of PDMS obtained from a commercial vendor (Sylgard 184, Dow Corning). Figure S4 shows the jig and the opposing convex and concave lenses (radius of curvature of 12.9 mm and diameter of 25.4 mm, CVI Laser Optics) used for this purpose. The convex lens was made of PDMS and was molded from the concave glass lens. Figure S5 provides a cross sectional illustration of the hemispherical transfer element with the important dimensions. Note the large, raised rim around the perimeter of the element (rim width is 1.5, 2.0 or 2.5 mm). This feature matches paddle arms in the tensioning stage described next. Figure S6 shows a top view illustration of the PDMS transfer element in its relaxed and tensioned state, with a to-scale illustration of the focal plane array overlaid.

Stretching the PDMS Transfer Element and Transfer Printing:

A specially designed radial tensioning stage provided a reproducible, controlled means to expand the hemispherical PDMS transfer element into a flat, drumhead state. Figure S7 provides a computer aided design drawing of this system based on a scroll plate design (design and drawing courtesy of Bill Knight, School of Chemical Sciences machine shop, UIUC). Ten separate paddle arms move in a coordinated fashion in the radial direction by an amount that can be controlled using a manual rotary stage. The raised rim of the PDMS element mounts onto the paddles. Figure S8 shows images of the stage and a transfer element in various stages of the stretching process. Figure S9 shows an image after liftoff of the array and removal from the tensioning stage, corresponding to the next to last frame in Fig. 1. Note that this array is a higher density array of passive silicon elements ($20 \times 20 \mu\text{m}$, with 50 nm thickness) and nearest neighbour connections ($20 \times 4 \mu\text{m}$, with 50 nm thickness).

The spatial distributions of the pixels in such an array are important to quantify and understand. Figure S10 shows in a sequence of frames corresponding to the process that we used to evaluate these distributions. A top view optical image (top frame) is converted to

binary format (middle frame), from which specially developed software locates the centers of the pixels and returns the coordinates (bottom frame).

Integrating with Hemispherical Cap and Imaging Lens:

Figure S11 shows cross sectional schematic illustrations and computer aided design drawings of the hemispherical cap and integrated imaging lens, with key dimensions. These components complete the cameras, but they do not represent critical design components.

Imaging with the Camera:

Mounting the focal plane arrays on specially designed printed circuit boards, forming interconnections and integrating with mux/demux electronics and software control systems enables image acquisition. For electrical connections to the circuit board, we used electron beam evaporation of Cr/Au through flexible shadow masks draped over the edge of the hemispherical camera substrate. Figure S12 shows the mux/demux electronics, and Fig. S13 provides a circuit diagram of these systems. The current responses at an applied bias of 4 V were measured for all the pixels in the 16 by 16 hemispherical camera used to generate the results of Fig. 3. See Fig. S14. Three different light intensities ranging from bright laser light (514.5 nm) to complete darkness have been used to test the detector arrays. A good range of sensitivity has been achieved for the photodetecting pixels, from current responses of 400~800 nA at the highest brightness to 0.5~2 nA in the dark state. Colourmaps illustrate the distribution of measured responses throughout the hemispherical detector array and highlight the response uniformity (two pixels with the non-ideal response of large current in the dark conditions are visible here). The greyscale images (e.g., Fig. 3d and Fig. 4a,b) represent the response signals for each pixel after normalization using the equation $Signal = \frac{I_{signal} - I_{min}}{I_{max} - I_{min}}$, where I_{signal} is the measured current at the exposure condition, I_{max} is the measured reference current at the brightest condition (maximum current), and I_{min} is the measured reference current at the dark condition (minimum current). Fig. S15 contains an electrical response

characterization of the pixels in the 16 by 16 planar camera; high pixel yields also were achieved in cameras with this geometry (3 out of 256 pixels have a less sensitive response).

Figure S16 demonstrates the optical setup used to image with the hemispherical detector. Green laser light (514.5 nm) was fed through an optical fiber to a fiber optics coupler and a beam expander (Thorlabs BE15M), and then onto a transparency film with an $\sim 1 \text{ cm}^2$ area printed image generated using a commercial laser printer (1200 dpi). The projected image passed through a plano-convex lens (Thorlabs BPX055) and onto the hemispherical electronic eye camera. Two rotating motors were used to scan the image over nearly the entire surface of the detector and maintain a eucentric point at the optical axis. The computer user interface used to capture images with the cameras was written in National Instruments LabView and is shown in Fig. S17. The maximum acquisition rate of the cameras (~ 1 frame per second) was limited by the control system and could be improved by adding more sophisticated electronics. The minimum acquisition time for an individual pixel was determined to be 15 ms as limited by the control electronics. The Supplementary Videos demonstrate the data acquisition process using a hemispherical camera (Video 1), as well as the detector rotations necessary to achieve higher resolution images (Video 2).

Figures S18 and S19 present the images acquired by each pixel in the hemispherical 16 by 16 detector array as they are scanned over the entire image. The camera scanned from -40 to 40° in both the θ and ϕ directions in 0.5° increments, with the center of the detector array positioned at $\theta=0^\circ$ and $\phi=0^\circ$. This 0.5° scanning resolution corresponds to ~ 7 -8 steps between pixels in the detector array. The yield of functioning pixels is high; only 2 out of 256 pixels, those at (row,column) positions (2,1) and (4,7), have a less sensitive response during imaging and should not be utilized.

Comparison of aberrations in hemispherical and planar detectors: Experiments

A comparison of focusing abilities for hemispherical and planar detectors required non-collimated light sources and a wide aperture for a large field of view. These two conditions allow imaging with light that is non-paraxial and simulates the standard operation mode of photographic cameras. The optical test setup for making the focusing comparison in Figs. 4c-4f used rear-illumination of a black and white pattern printed on paper with halogen lamps. A pair of optical filters limited the incident light wavelength to ~620-700 nm and minimized contributions from chromatic aberrations. The paper aided in diffusion of the light from the lamps. A high numerical aperture plano-convex lens (Edmund Optics PCX NT45-083; diameter=12 mm; focal length=12 mm) was used for the imaging optics with the convex side towards the light source. The lens to object distance was fixed at 62.85 mm.

Two types of planar screens were used to demonstrate the curvilinear shape of the optimal focal surface. Figure S20 shows high resolution photographs of the projected images on a planar screen (35 mm photographic plastic film) obtained using a commercial camera (Canon EOS30D with a Canon Macro Lens EF 100mm f/1:2.8 USM). Figure S21 contains images acquired using the fabricated planar cameras (16 by 16 pixels) when scanned in the x and y directions from -460 to 460 μm in 92 μm increments. A series of such images were collected for detector to lens (planar side) distances ranging from 5.85 to 22.05 mm. The position of best focus shifts from the center to the edge of the image with decreasing detector to lens distance, thereby indicating that the optimal focal surface is highly curved and non-planar.

The fabricated hemispherical camera (16 by 16 pixels) was also used to image this same setup at varying positions along the optical axis (Fig. S22). Scanning of the detector from -2 to 2° in both the θ and ϕ directions in 0.4° increments followed by image reconstruction generated high resolution photographs. The quality of focus obtained is consistent throughout each image, with an optimal focus being achieved for the detector

position $z \approx 16.65$ mm. The hemispherical detector surface provides improved imaging compared to planar detectors with better focusing, fewer distortions, and a wider field of view.

Comparison of aberrations in hemispherical and planar detectors: Theory

The laws of geometric optics allow for single planar or curved object surfaces to be imaged perfectly onto a curved image plane, though the image may be distorted.¹ Distortion is a purely geometric effect that does not influence the sharpness of the images and can be removed.¹ We performed ray tracing analysis with a commercial software program (Rayica) to compare distortions and defocusing on the fabricated hemispherical and planar detectors.² The rays passed through a plano-convex lens (Edmund Optics PCX NT45-803) and onto the screens. An approximation to the optimal image surface was constructed by fitting a paraboloid of revolution, with a general form of $z = 16.65 - 0.105r^2$, to the locations of the smallest focal spots (the root mean square of the intensity was minimized) formed by a set of point objects arrayed on a line through the focal surface. Although the fabricated hemispherical detectors and the optics are not matched to achieve perfect imaging, significant reductions in both distortion and defocusing over planar detectors were observed.

The single lens system is perhaps the simplest example of how a curved detector could be used to improve camera performance. Since flat electronic detectors were introduced, there has been a trend to design both the optics and signal processing of cameras in an integrated manner, even to the extent that the signal recorded by the detector may not be recognizable as an image before processing.³ We expect our fabrication technique, which removes the design restriction that the detector arrays be planar, to allow simplifications and further optimizations to be made.

Mapping of Silicon Elements onto a Hemisphere:

A simple mechanics model, based on plate theory,⁴ and confirmed using established finite element analysis techniques,^{5,6} shows how the silicon elements are mapped from the flat to hemispherical surfaces. Figure S23 illustrates the mapping of silicon elements onto a hemisphere. A PDMS hemispherical cap of radius R (Fig. S23a) is first stretched to a flat plate of radius r_1 (Fig. S23b), which is further stretched to radius r_2 (Fig. S23c) to transfer the silicon elements of size L_{Si} and spacing L_0 (Fig. S23d). The release of tension first leads to an approximately flat plate of radius r_1' (Fig. S23e), and the further release leads to a new hemisphere of radius R' (Fig. S23f).

The above mapping process has been studied via the finite element method. Shell elements are used to model the PDMS hemispherical cap. Figure S24a shows the original mesh for the PDMS hemispherical cap in Fig. S23a, while Fig. S24b shows the deformed mesh when the hemisphere is just flattened to a plate (when the edge of deformed hemisphere approximately reaches the same height as the plate center), corresponding to Fig. S23b. The (axisymmetric) strain distribution in the flattened plate shown in Fig. S24c clearly suggests that the meridional strain is negligible (\ll circumferential strain), $\varepsilon_{\text{meridional}} \approx 0$. This gives the arc length $R\varphi$ of the hemisphere to be the same as the radius r_1 of the flattened plate, $R\varphi = r_1$. This is validated by the finite element analysis shown in Fig. S24d. The circumferential strain is then given by $\varepsilon_{\text{circumferential}} \approx \frac{\varphi - \sin \varphi}{\sin \varphi}$, which agrees well with the finite element analysis, as shown in Fig. S24c.

The additional strains due to further stretching in Fig. S23c are uniform throughout the plate. The transfer of silicon elements in Fig. S23d do not introduce any strains.

Since the Young's modulus of silicon (130GPa) is 5 orders of magnitude stiffer than the Young's modulus of PDMS (2MPa), the strains in silicon elements are rather small, which prevents the PDMS underneath the silicon elements from being released during the relaxation to the flat stage shown in Fig. S23e. For PDMS not covered by the silicon elements, its length is reduced from L_0 to $\frac{r_1}{r_2} L_0$. Therefore the radius of relaxed plate in Fig. S23e becomes

$r_1' = \frac{L_{Si}r_2 + L_0r_1}{L_{Si} + L_0}$. For the hemispherical PDMS transfer element in Fig. S5 and $L_{Si} = 500\mu m$, $L_0 = 420\mu m$, the above formula gives $r_1' = 7.83mm$, which agrees well with the radius $r_1' = 7.71mm$ obtained by the finite element method to model the PDMS and silicon by the shell. Figure S25a shows the deformed shape of the flat, relaxed PDMS and silicon corresponding to the state in Fig. S23e.

For the further release to the hemispherical cap (corresponding to Fig. S23f), Fig. S25b gives the deformed shape of the spherical, relaxed PDMS and silicon. It is approximately a hemisphere with slightly larger radius $R' = 13.4mm$ due to the stiffening effect of silicon elements. The mechanics analysis gives the new radius $R' = R(1-f)\left(1 + \frac{f}{1-f}\frac{r_2}{r_1}\right)^{3/2}$, which is $R' = 14.3mm$, and agrees reasonably well the finite element analysis, where $f = \frac{NL_{Si}^2}{\pi r_2^2}$

is the area fraction of the silicon elements on the PDMS surface, and N is the number of silicon elements.

Figure S26 shows the images obtained by the finite element method of the mapping process schematically illustrated in Fig. S23. Figure S27 shows the spatial distribution of elements in a 16 by 16 array transferred to a hemispherical PDMS element as predicted by the mechanics model and as measured during fabrication (see Fig. S10). The pixel positions given by the mechanical models agree well with the experiments without parameter fitting. These mechanics models indicate very small, $\sim 3\%$, changes (maximum to minimum) in the local pitch across the entire area, with smooth, deterministic variations in this quantity. The relatively uniform pitch is $\sim 10\%$ smaller than the initial value before the PDMS is relaxed.

Arc-Shaped Connections between Silicon Elements:

The nature of the compressibility provided by the narrow, thin interconnects between adjacent unit cells also can be understood through theoretical analysis (see Fig. S28). The SEM image in Fig. S29 provides a high magnification view of a unit cell in a high-density passive Si array transferred to a hemispherical surface (from Fig. S9), with analysis results in the form of color overlays of the arc shapes and the distributions of strain. The out-of-plane displacement, w , of the arc-shaped connections takes the form $w = \frac{A}{2} \left(1 + \cos \frac{2\pi x}{L} \right)$, where A is the amplitude, x is the position along the connection and L is the lateral separation distance between adjacent pixel elements. The distance $L_0 = 20 \mu\text{m}$ is measured in the as-fabricated planar configuration. This equation satisfies vanishing displacement and slope at the two ends ($x = \pm L/2$). The in-plane displacement can then be obtained from the force equilibrium.

These give the bending energy $U_b = \frac{\pi^4 E h^3 A^2}{12(1-\nu^2)L_0^3}$ and membrane energy

$$U_m = \frac{E h L_0}{2(1-\nu^2)} \left(\frac{\pi^2 A^2}{4L_0^2} - \frac{L_0 - L}{L_0} \right)^2. \quad \text{Energy minimization } \frac{\partial(U_b + U_m)}{\partial A} = 0 \text{ gives the}$$

amplitude A yields an analytical expression for the amplitude $A = \frac{2L_0}{\pi} \sqrt{\frac{L_0 - L}{L_0} - \varepsilon_c}$, where, ε_c , the critical buckling strain, is given by $\varepsilon_c = \pi^2 h^2 / (3L_0^2)$, where h is the thickness; its value is 0.0021% for the system shown here. For $L = 17.5 \mu\text{m}$, the amplitude $A = 4.50 \mu\text{m}$ agrees well with the experiments $A = 4.76 \mu\text{m}$. The maximum strain in the connections is $\sim 0.5\%$, substantially below the fracture strain for the silicon.

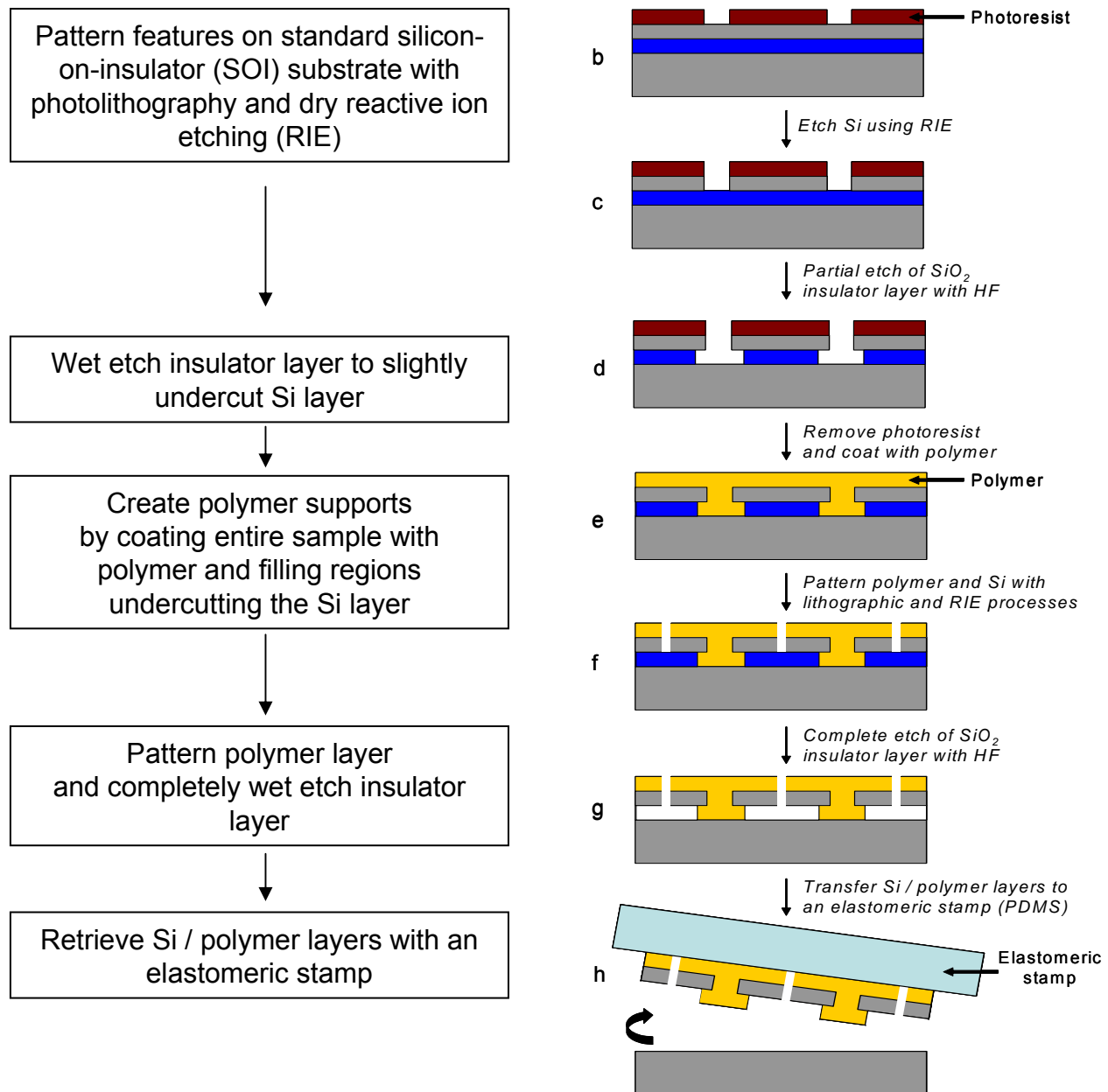
Strain Distributions in Silicon Elements:

Mechanics models can also reveal the distribution of strains and displacements in the square silicon elements. As shown in Fig. S28b, the out-of-plane displacements in connections impose bending moments M (and axial force F) to the silicon elements, which are modelled as two-dimensional plates. The bending energy in the silicon elements is obtained in terms of its out-of-plane displacement w via the plate theory. The PDMS substrate is

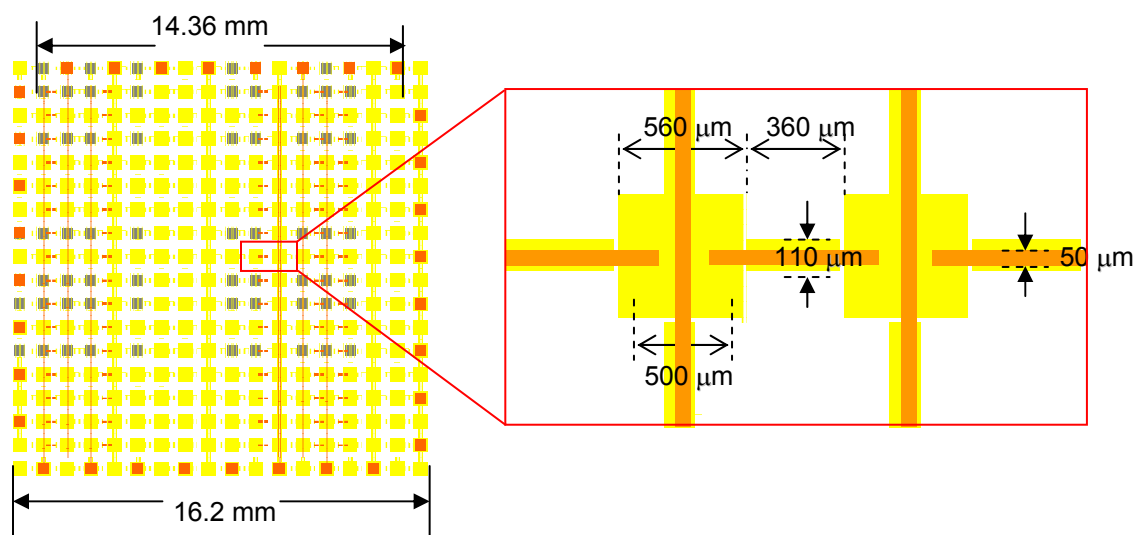
modelled as a semi-infinite solid subjected to the surface displacement w , and its strain energy is also obtained in terms of w . The displacement w can be expanded to the Fourier series, with the coefficients to be determined by minimizing the total energy. The bending strains in silicon elements can then be obtained from the curvatures, which are the second order derivatives of w . The maximum out-of-plane displacements are very small ($< 0.1\mu\text{m}$), as are the strains ε_{xx} and ε_{yy} ($< 0.08\%$), as shown in Fig. S29. The strain ε_{xx} in the Si element reaches the peak near the interconnections in the x -direction, while the peak of ε_{yy} occurs near those in the y -direction.

REFERENCES:

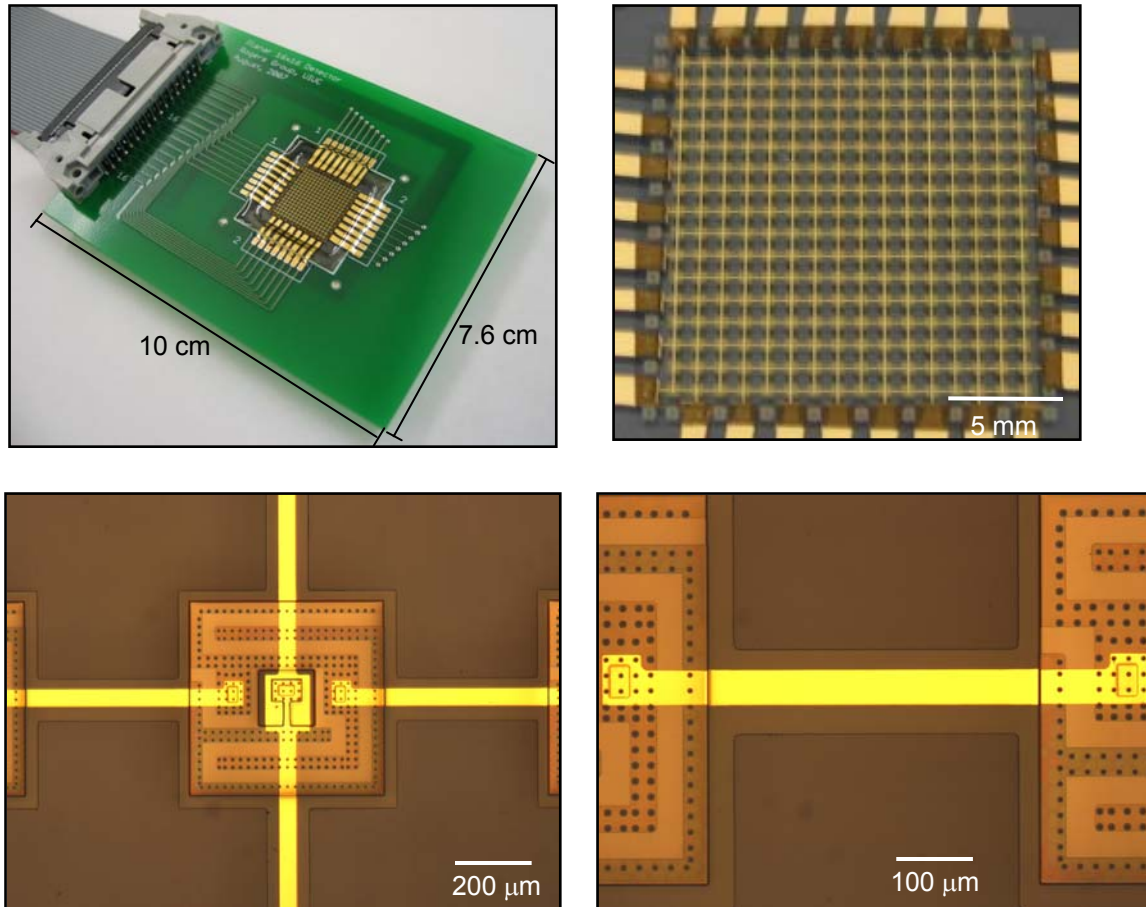
1. Walther, A. The Ray and Wave Theory of Lenses, Cambridge University Press, Cambridge, UK (1995).
2. Rayica 3.0, Optica Software, Champaign, IL, USA (2007).
Mathematica 6.01, Wolfram Research, Champaign, IL, USA (2007).
3. Mait, J. N., Athale, R. & van der Gracht, J. Evolutionary paths in imaging and recent trends, *Opt. Express* **18**, 2093-2101 (2003).
4. Timoshenko, S. Theory of Plates and Shells. McGraw-Hill, New York (1940).
5. Belytschko, T., Liu, W. K. & Moran, B. Nonlinear Finite Elements for Continua and Structures. Wiley, New York (2000).
6. ABAQUS Inc., ABAQUS Analysis User's Manual V6.5 (2004).



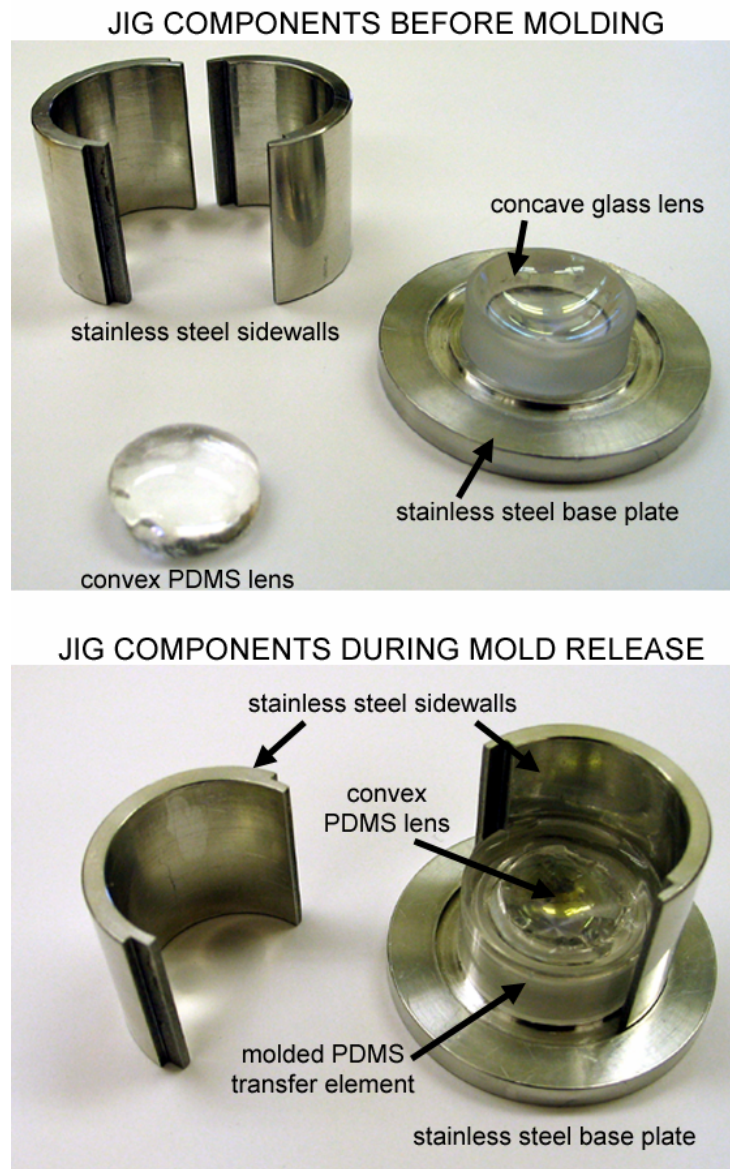
Supplementary Figure S1: Process flow for efficient removal of the focal plane array from the SOI wafer. The key steps are **d-h**, in which a spin cast layer of polymer (polyimide for the results presented here) penetrates through predefined etch holes to keep most of the array suspended from the underlying silicon handle wafer after HF undercut etching of the buried oxide. This strategy avoids stiction that would otherwise frustrate the ability to lift off the array. The posts formed by the polymer prevent unwanted slipping or wrinkling of the array during the HF etching.



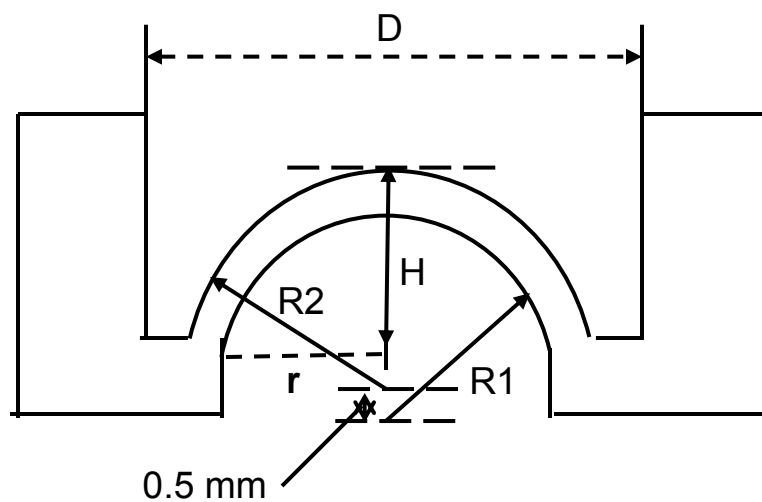
Supplementary Figure S2: Schematic illustration of the layout of the focal plane array, with key dimensions indicated. The light brown, dark brown and grey regions correspond to polyimide, Cr/Au and silicon, respectively.



Supplementary Figure S3: Photographs (top frames) and optical micrographs (bottom frames) of a planar camera that uses processing approaches, focal plane array designs, interconnect schemes and other features similar to those used for the hemispherical camera. This system was used to evaluate various aspects of the designs and fabrication techniques. These images provide views of certain features that are difficult to show clearly in the hemispherical geometry, due to limited depth of focus associated with optical microscopes.

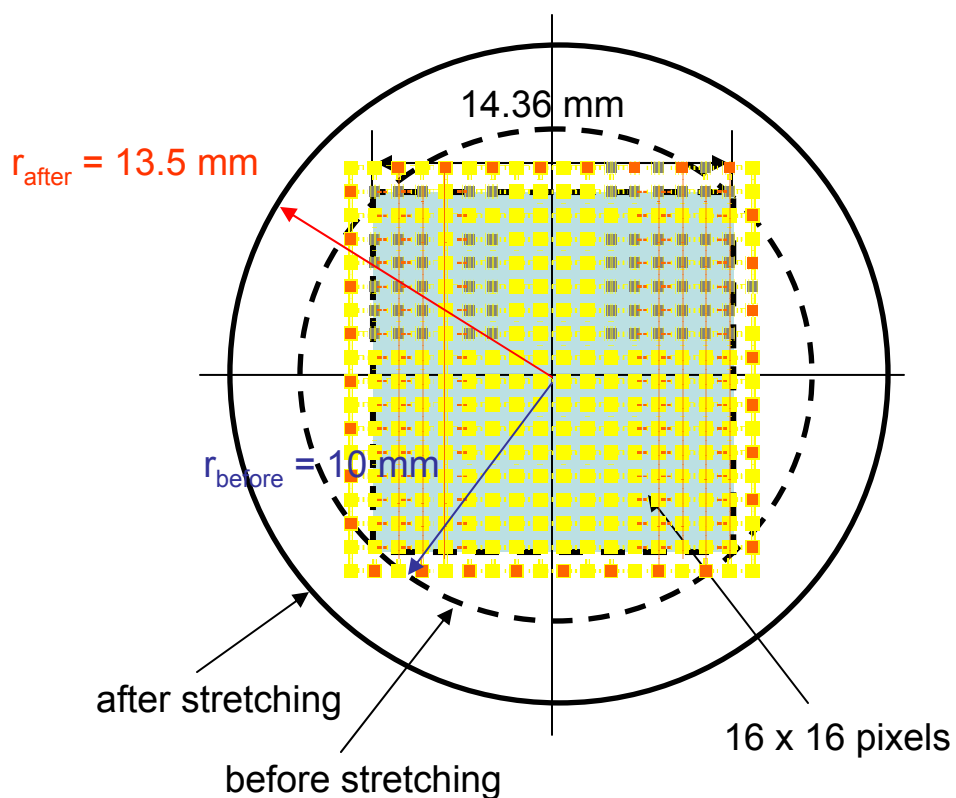


Supplementary Figure S4: Optical images of the mounting jig used for casting and curing the hemispherical PDMS transfer elements.

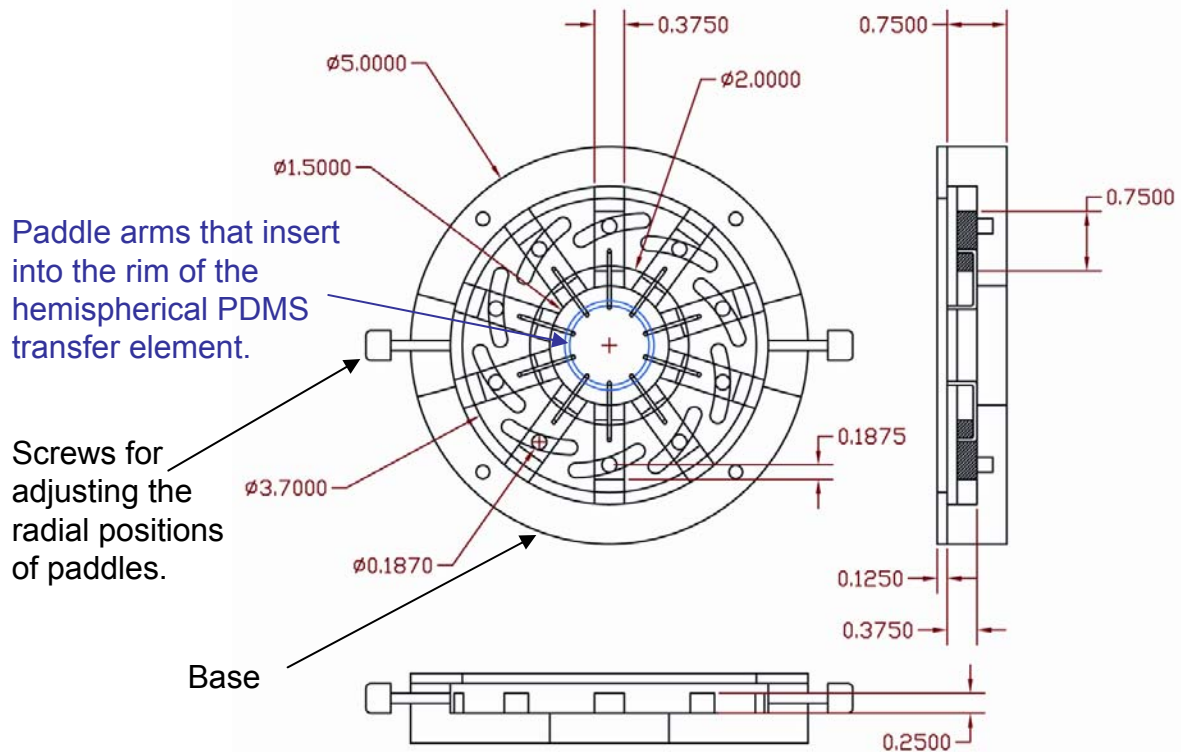


$R1$ and $R2 = 12.9\text{ mm}$, $H = 5\text{ mm}$
PDMS thickness at center $\sim 0.5\text{ mm}$
 $D = 25.4\text{ mm}$

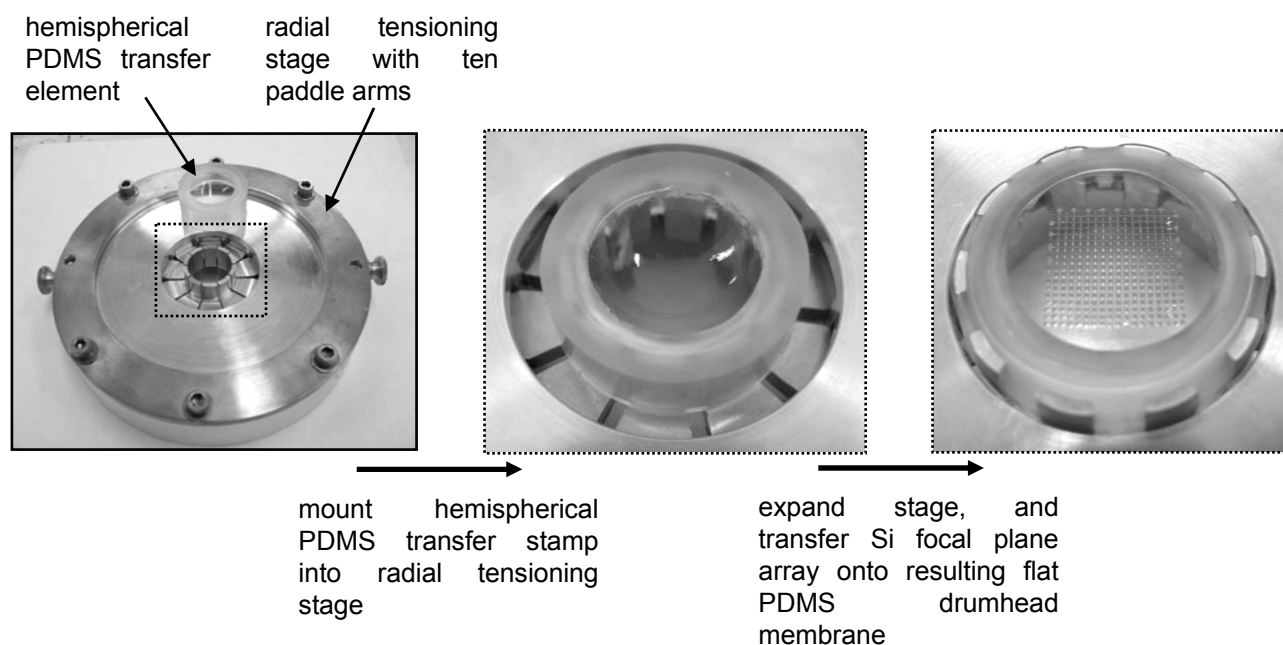
Supplementary Figure S5: Cross sectional schematic illustration of the layout of the hemispherical PDMS transfer element, with key dimensions.



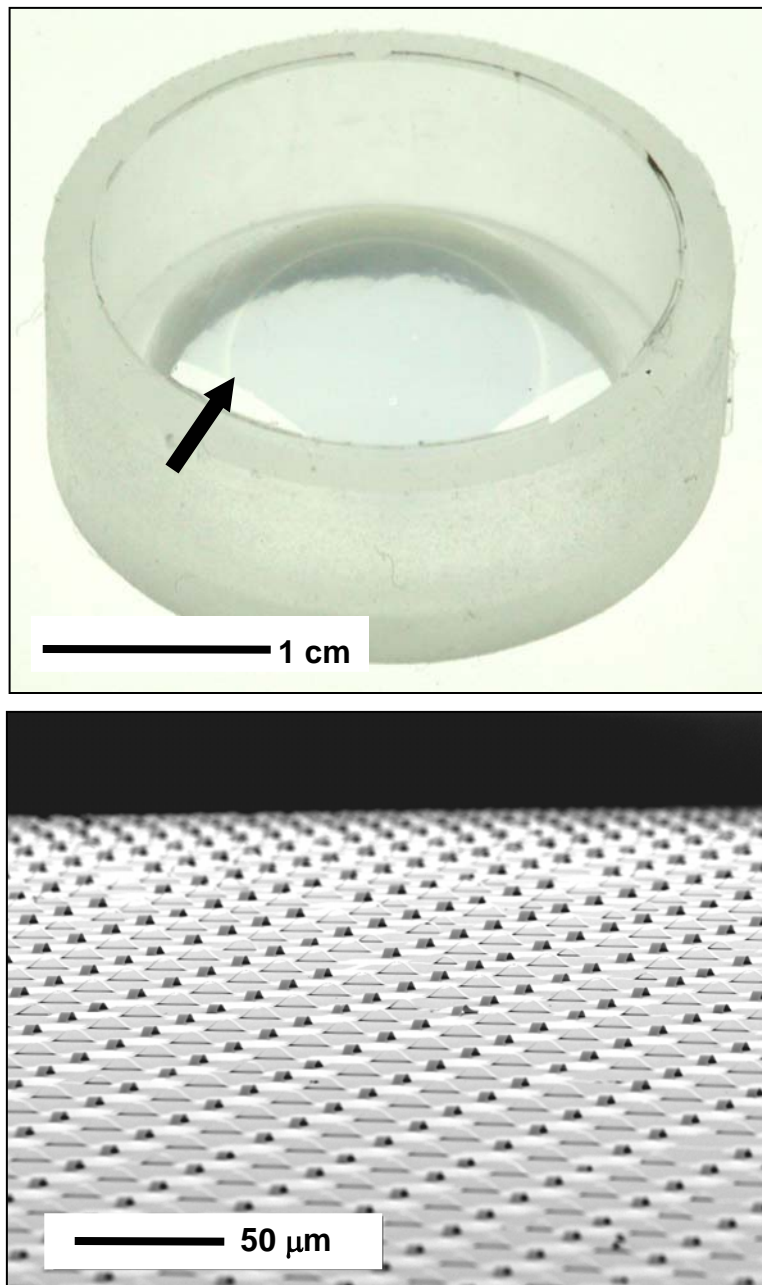
Supplementary Figure S6: Top view schematic illustration of the layout of the hemispherical PDMS transfer element, with key dimensions in the as-fabricated and radially tensioned configurations. An overlay in the center portion of this image shows the layout of the passive matrix array, illustrated to scale.



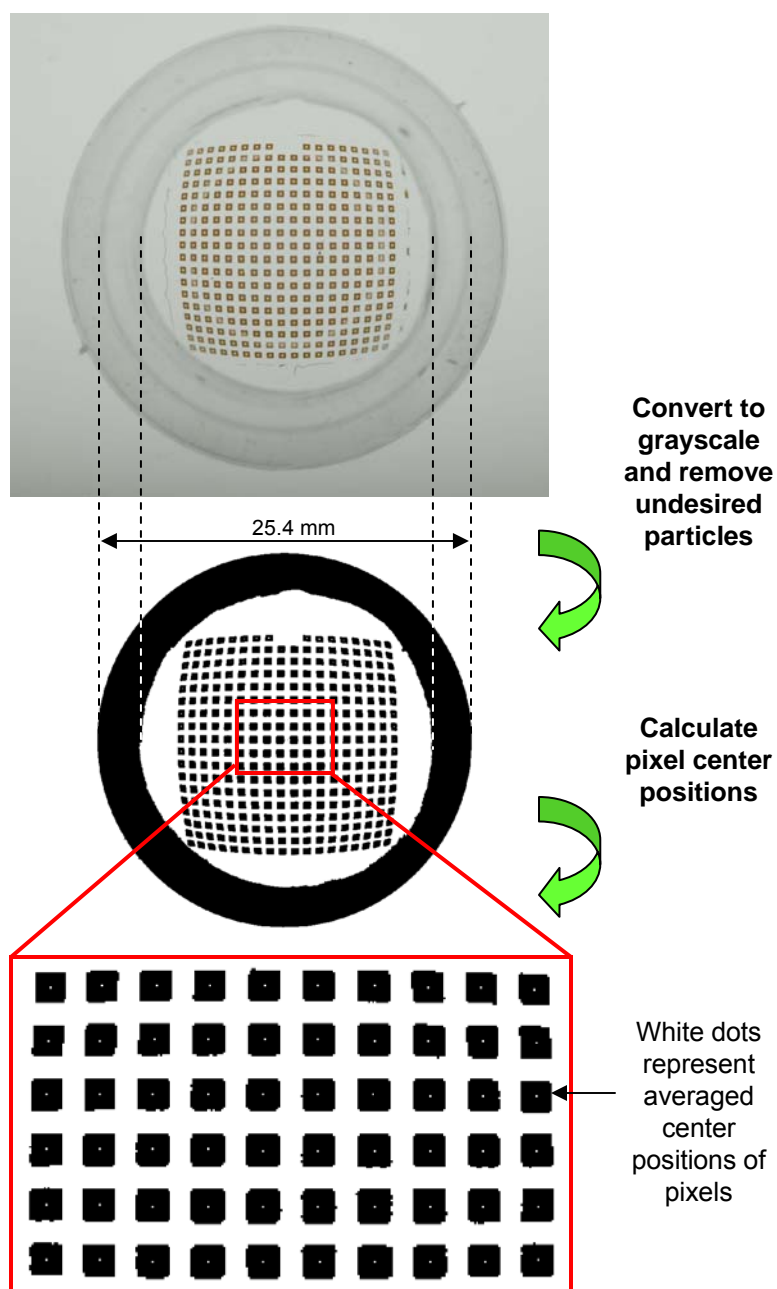
Supplementary Figure S7: Computer aided design drawing of the radial tensioning stage. The hemispherical PDMS element mounts in the center. The paddle arms move radially to expand the hemisphere into a planar drumhead shape.



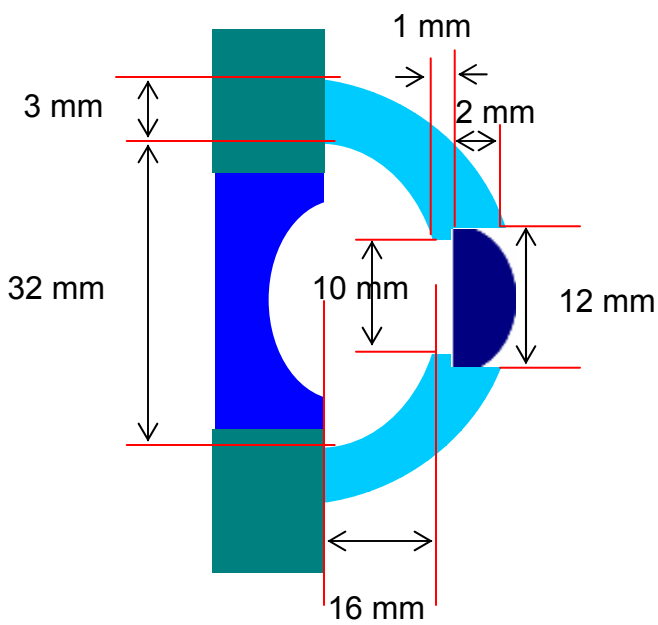
Supplementary Figure S8: Photograph of radial tensoning stage and PDMS transfer element (left frame). PDMS element mounted on the paddle arms of the stage (center frame), corresponding to the region of the image on the left indicated with a dashed line box. The right frame shows the PDMS element in its flat, drumhead configuration with a focal plane array on its surface.



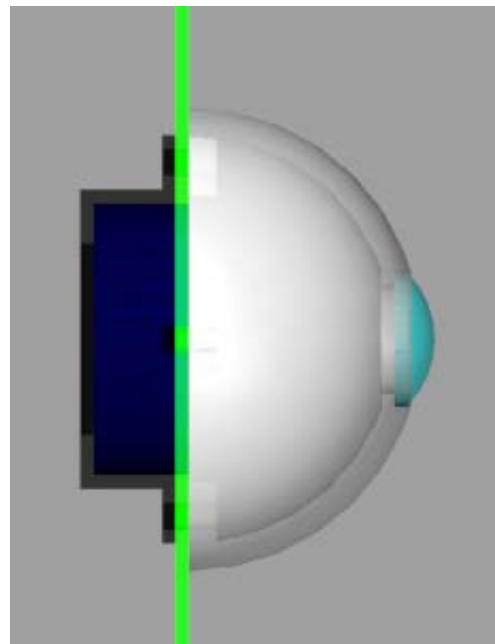
Supplementary Figure S9: Photograph of a compressible silicon structure on a PDMS hemisphere (center; a tall, raised rim lies around the perimeter) (top image). The silicon covers the central region of the hemisphere, and appears light grey in this image; the straight edges of the overall structure can be seen clearly (arrow). This system consists of 163,216 square elements of silicon (20 by 20 mm; 50 nm thick) connected by ribbons of silicon (20 by 4 mm; 50 nm thick) in a 16.14 by 16.14 mm square array, initially formed on the planar surface of a silicon-on-insulator wafer. A scanning electron micrograph (SEM) of a small region of the sample is shown in the bottom image. The out-of-plane deformations in the connecting ribbons that yield the arc shapes visible here provide the compressibility necessary to accommodate the planar to hemispherical transformation.



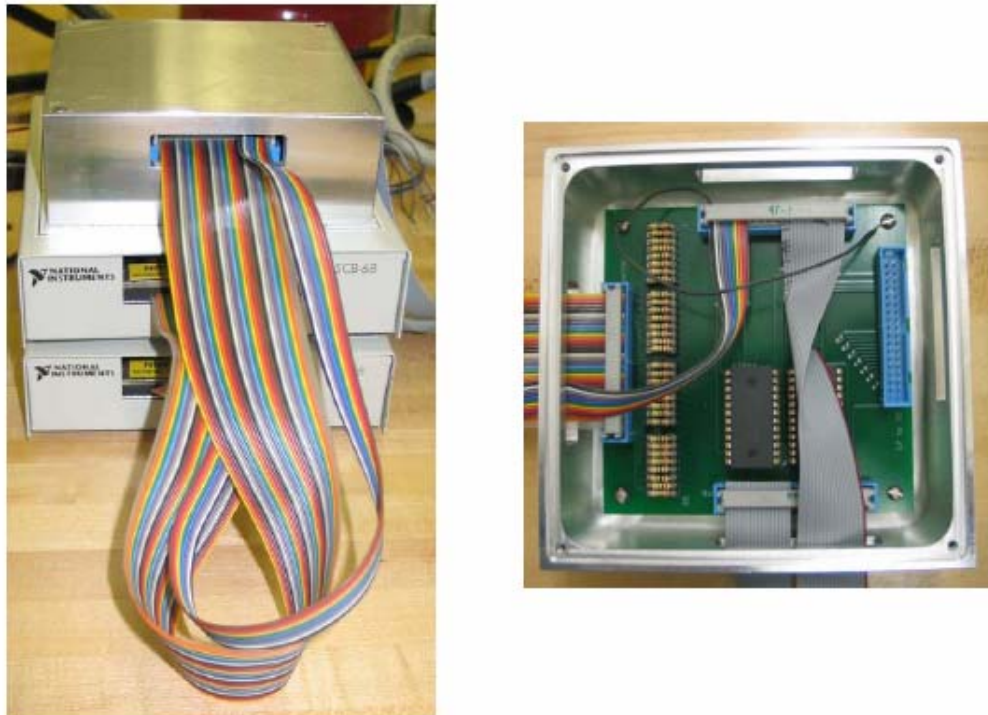
Supplementary Figure S10: Procedures for evaluating the spatial distributions of the pixel elements in a hemispherical focal plane array on a glass substrate. The process starts with a photograph of the system (top frame) that is then converted into a binary format (center frame) and then manipulated with imaging processing software to locate the spatial coordinates of the centers of the pixels.



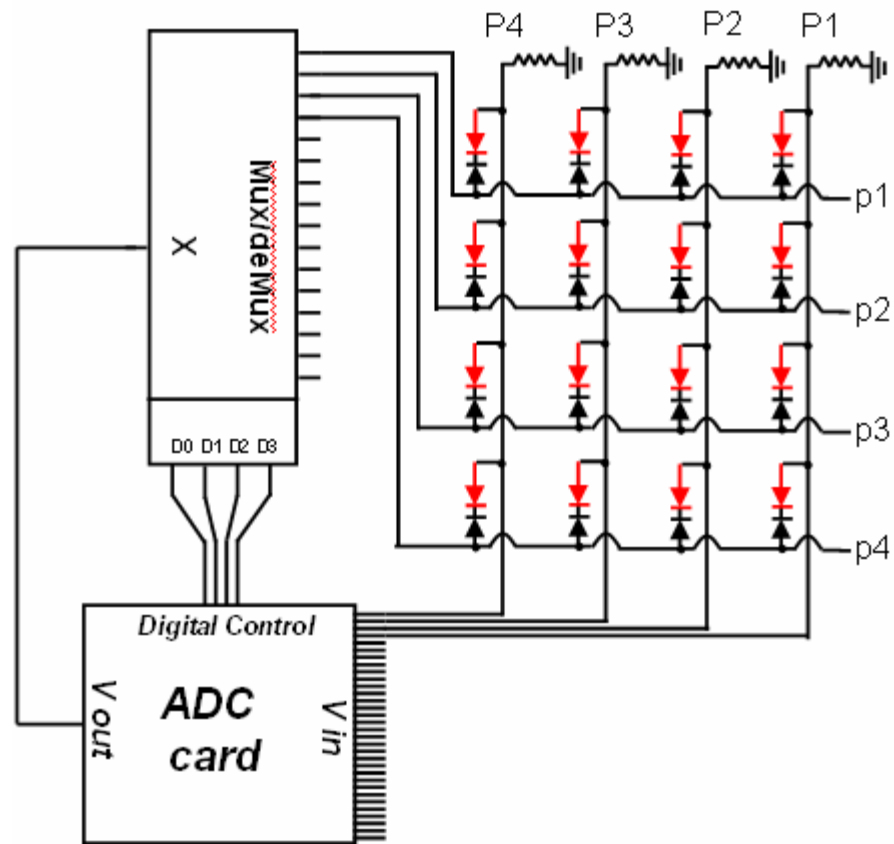
detector curvature
 $R=12.9$ mm



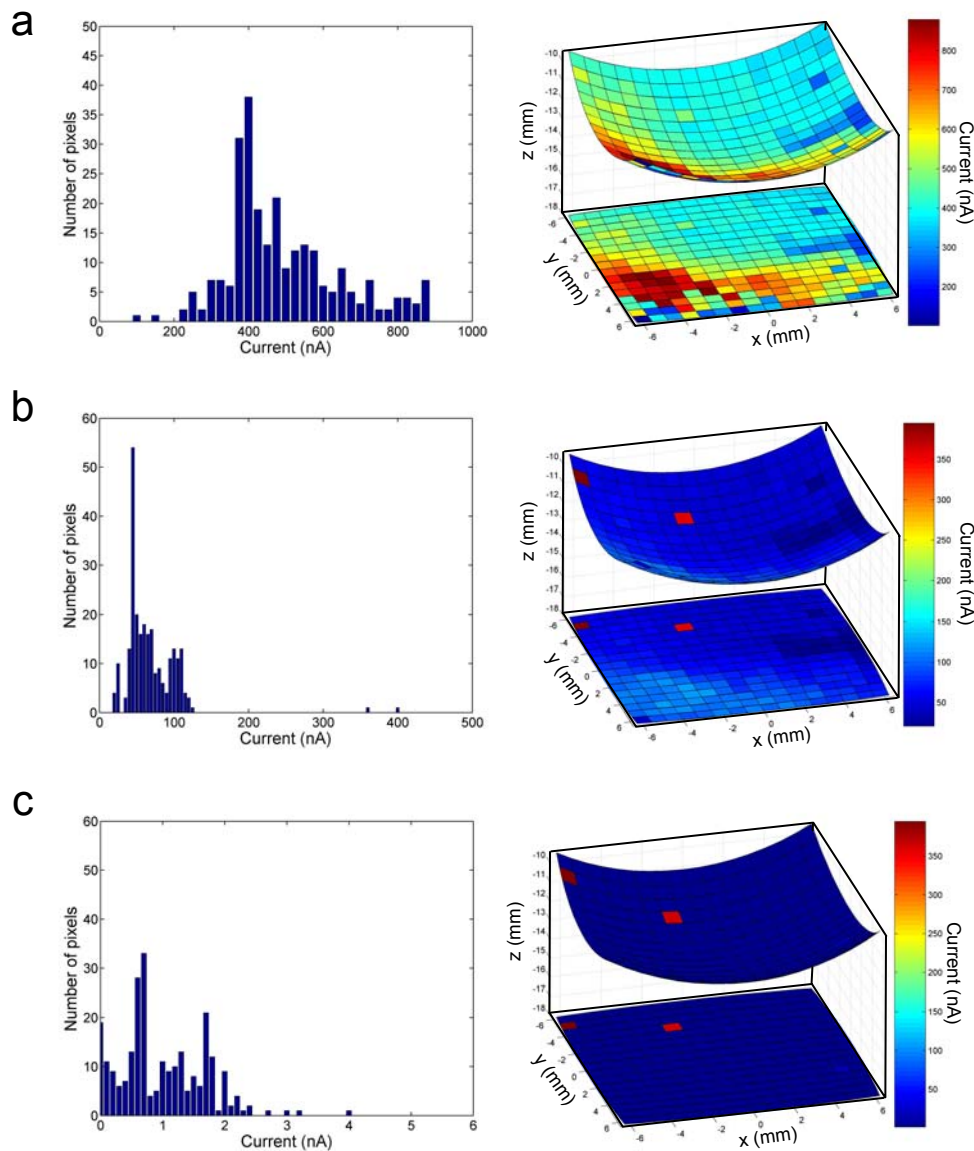
Supplementary Figure S11: Cross sectional schematic illustration and computer aided design drawing of the spherical cap and imaging lens, with key dimensions.



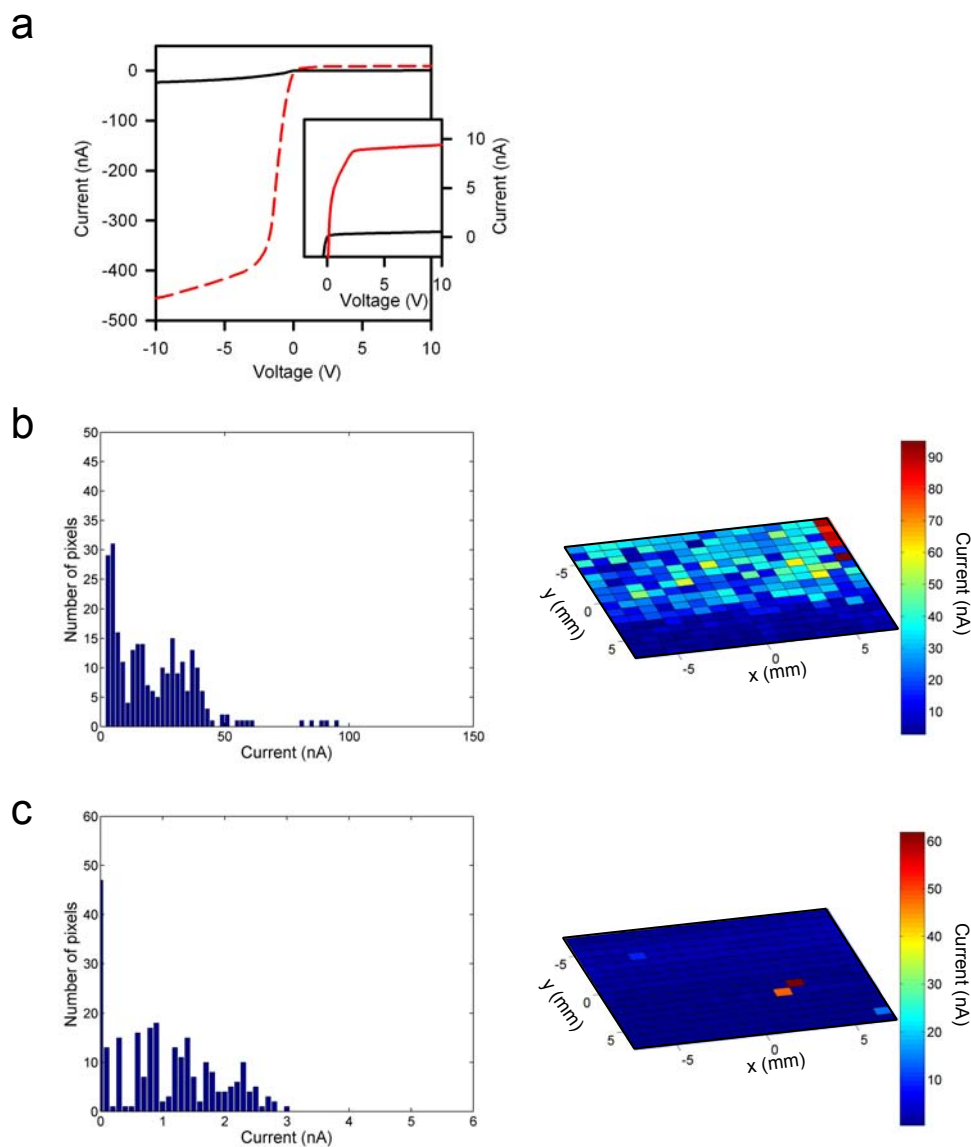
Supplementary Figure S12: Photograph of the mux/demux system for image acquisition.



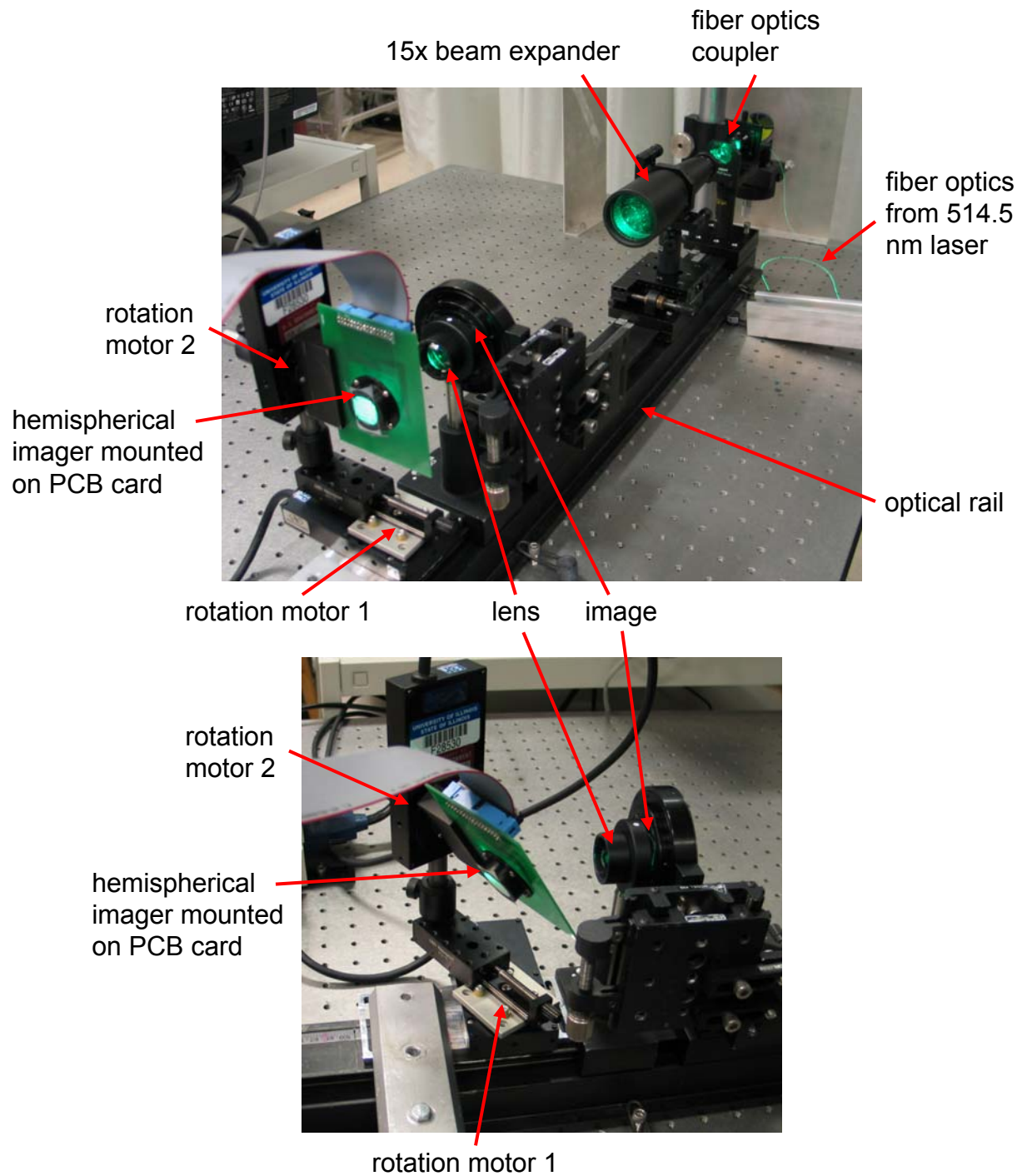
Supplementary Figure S13: Circuit diagram for the electronics for image acquisition.



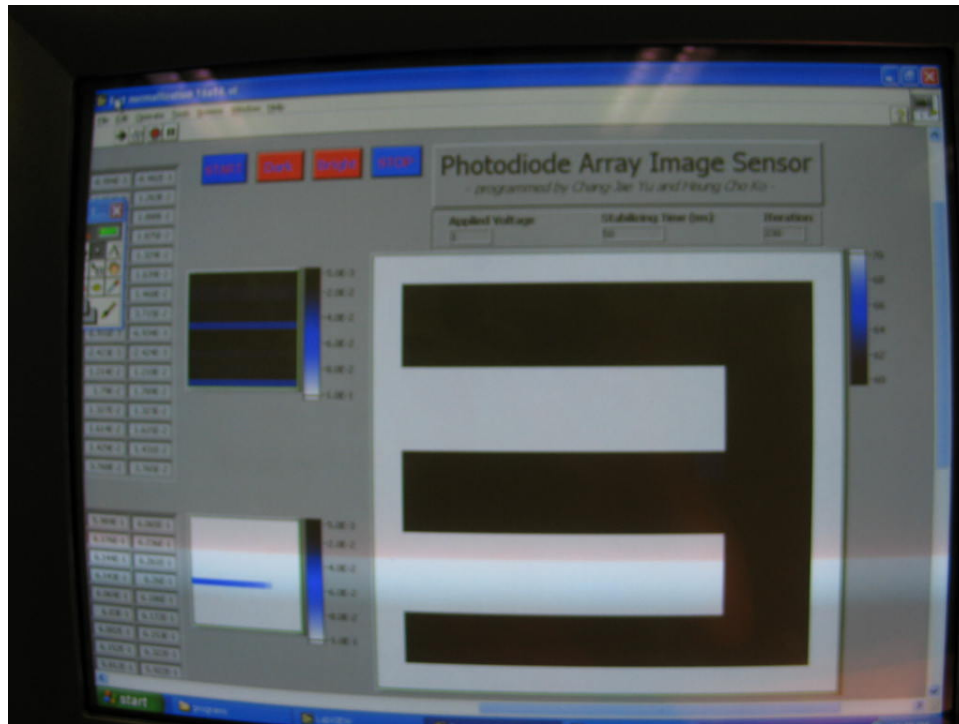
Supplementary Figure S14: Optoelectronic response of the 16 by 16 pixel photodetector array in a hemispherical camera. The current responses at an applied bias of 4 V have been measured for all the pixels at three different light intensities, including **a**, brightest laser light (514.5 nm), **b**, approximately one-tenth of the bright case, and **c**, complete darkness. The histograms on the left show the distribution of pixels with a given current response, while the colourmaps on the right show the mapping of pixels with a given response in the hemispherical camera.



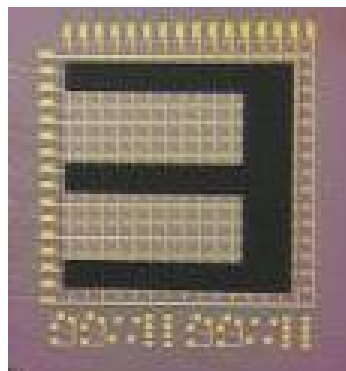
Supplementary Figure S15: Optoelectronic response of the 16 by 16 pixel photodetector array in a planar camera. **a**, Electrical properties of a unit cell. The data were measured by contacting the row and column electrodes that address this position in the hemispherical array, via pads at the perimeter of the system. The data (red: exposed to light; black: in the dark) show high contrast response to light exposure. The current responses at an applied bias of 4 V have been measured for all the pixels at two different light intensities, including **b**, bright case with a sheet of white paper backlit with halogen lamps and optically filtered to 620~700 nm wavelengths (identical setup used to generate Fig. 4e-g), and **c**, complete darkness. The histograms on the left show the distribution of pixels with a given current response, while the colourmaps on the right show the mapping of pixels with a given response in the hemispherical camera.



Supplementary Figure S16: Photographs of the optical setup used for image acquisition.

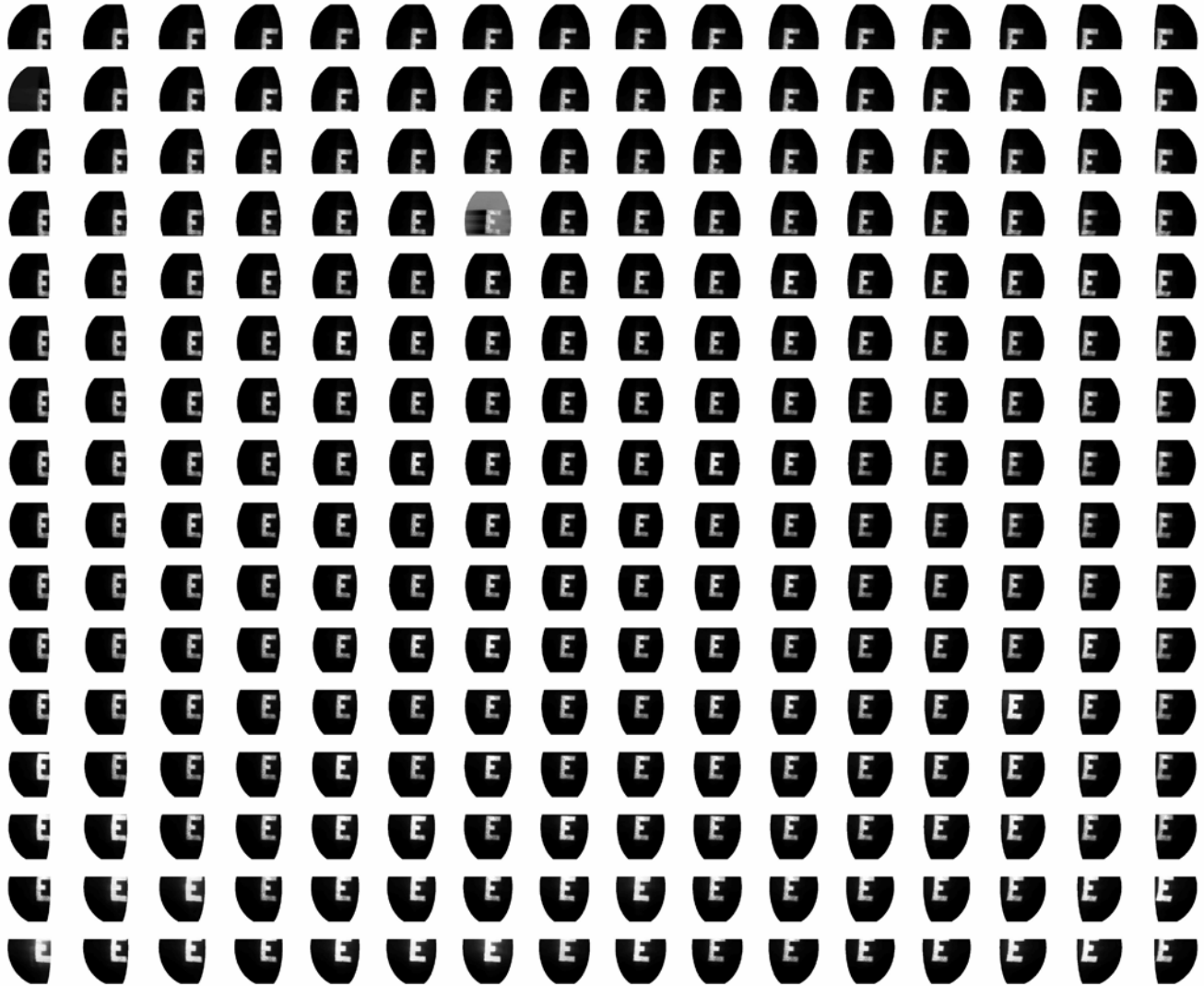


Screen capture of the Labview interface used for imaging.

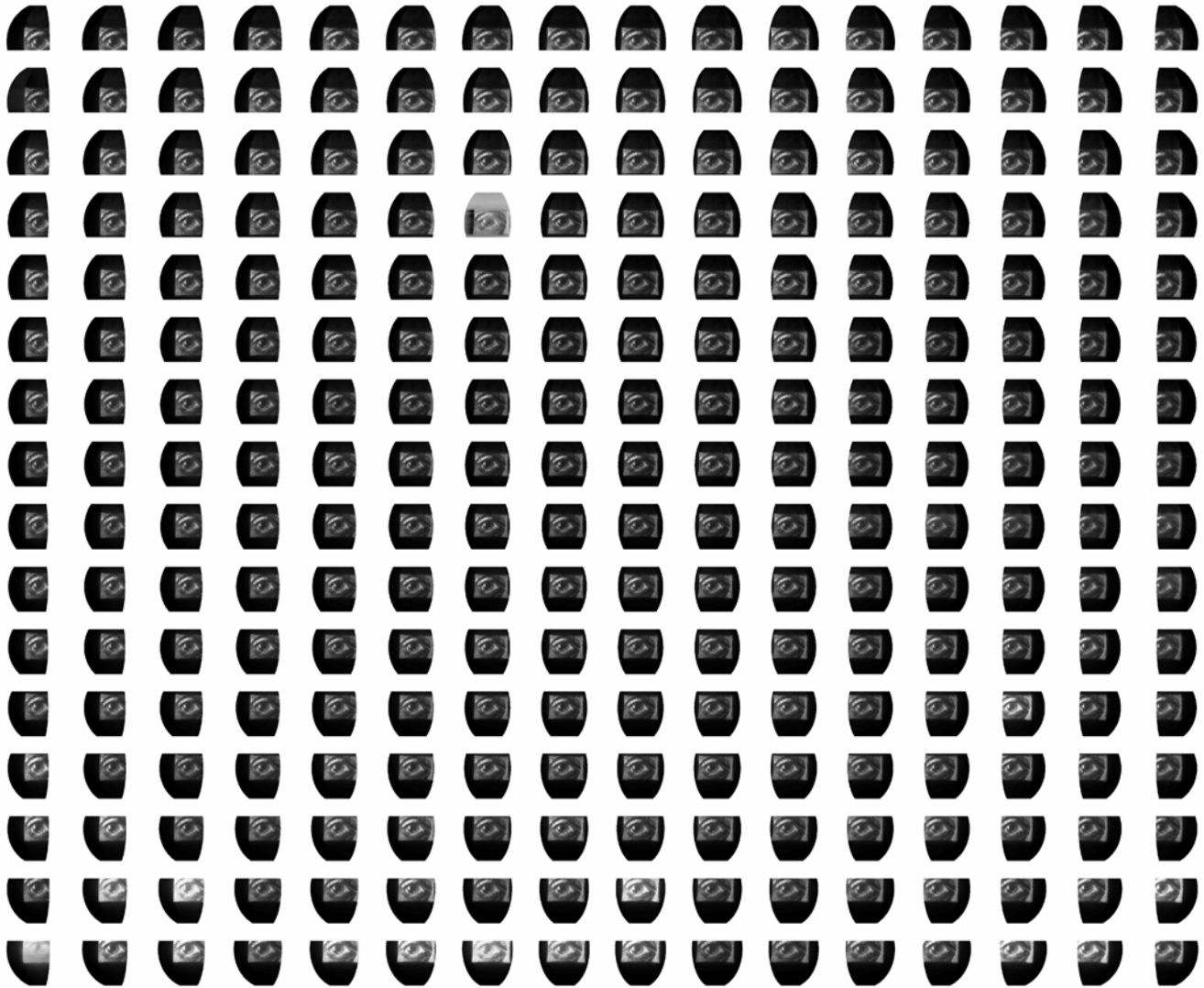


Photograph of 16x16 focal plane array with overlaid **E** printed on transparency.

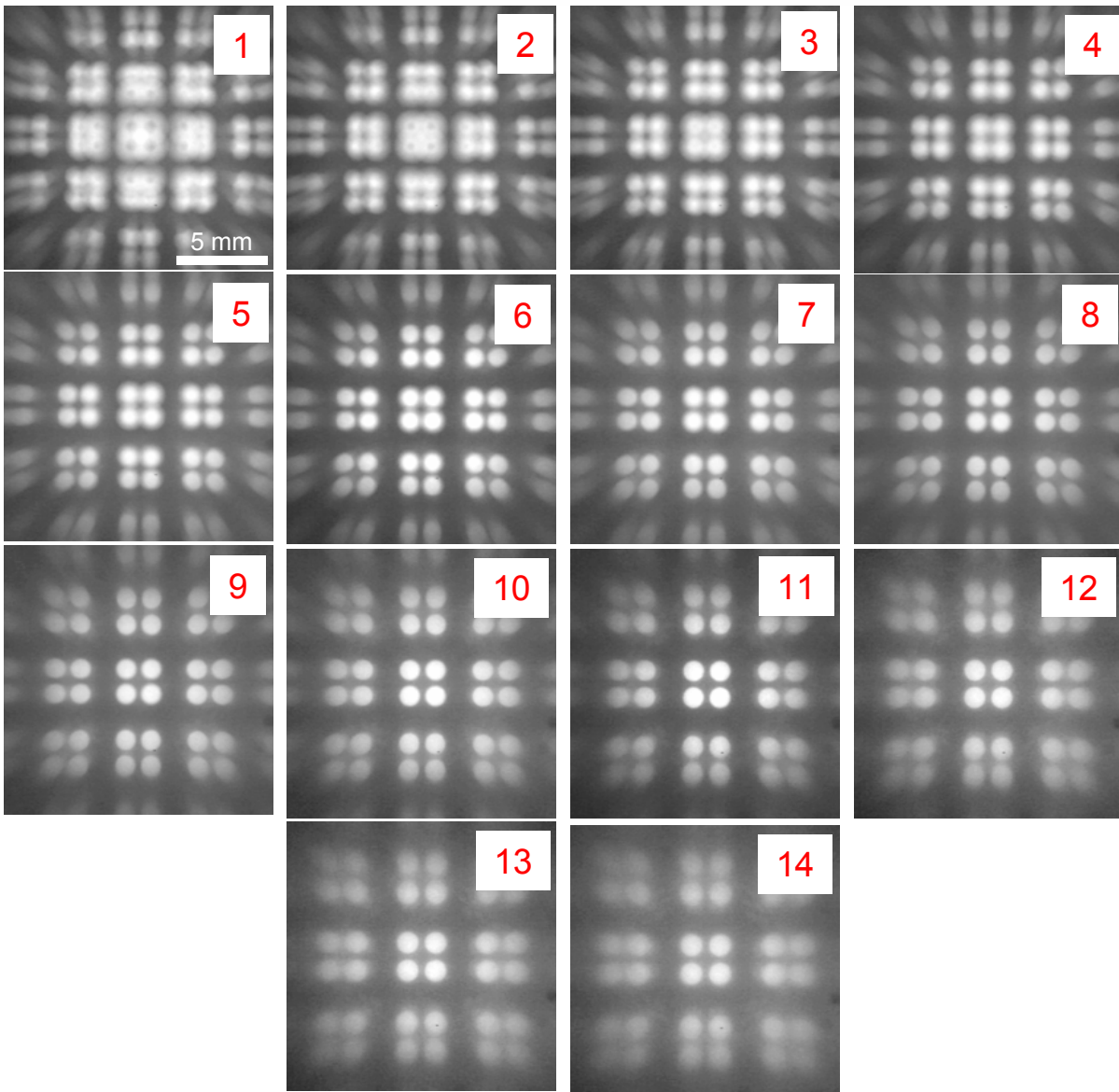
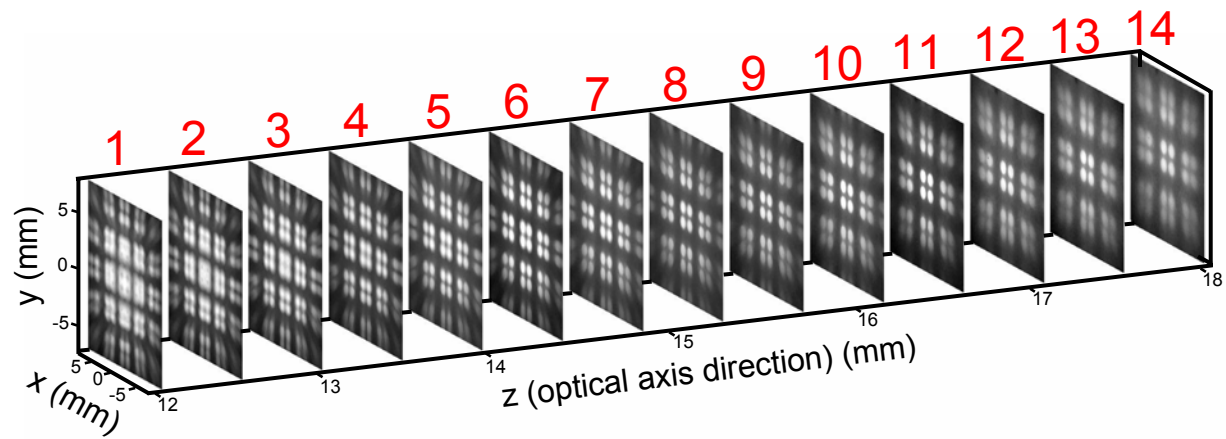
Supplementary Figure S17: Screen capture for the software interface used for imaging.



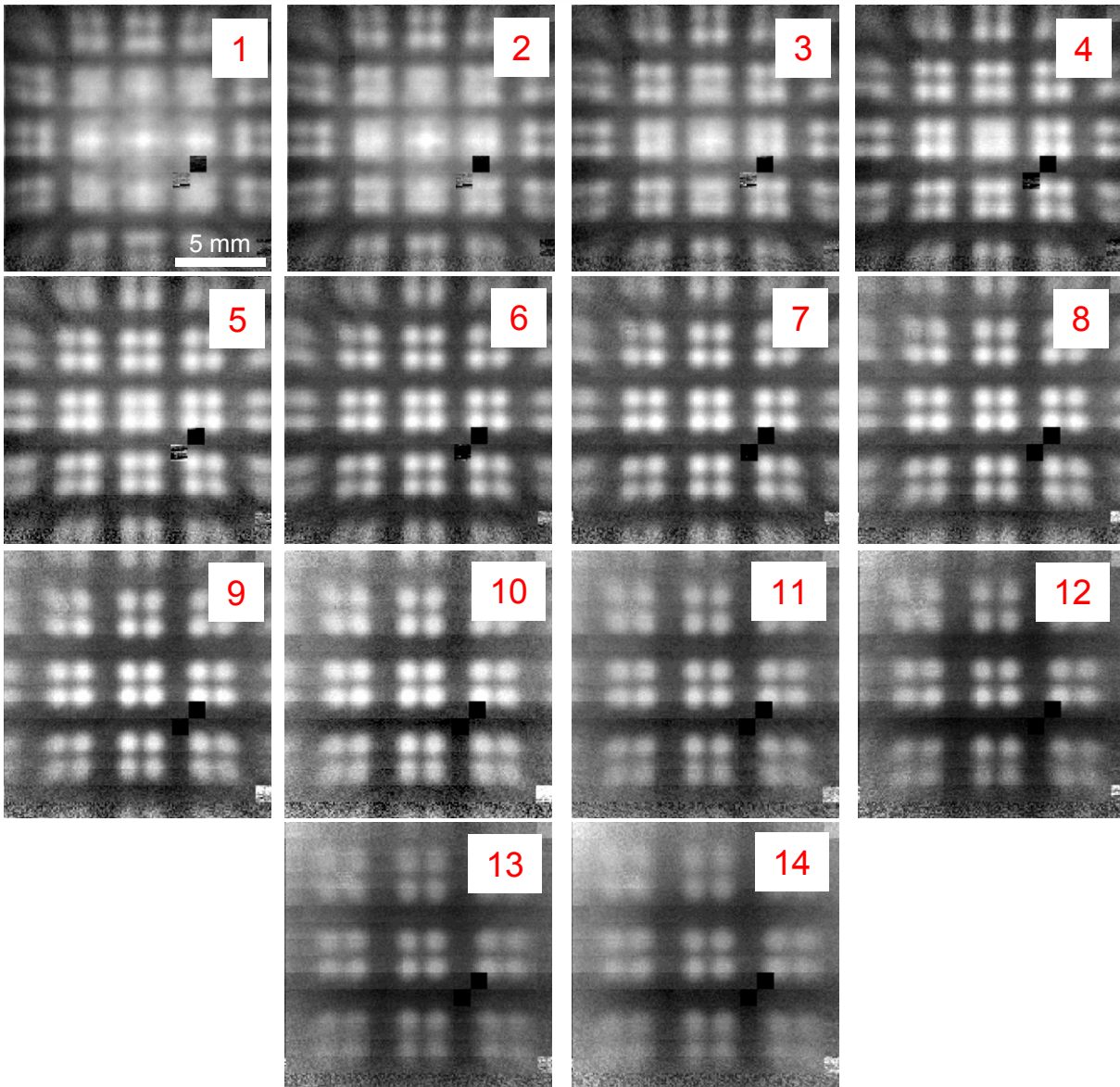
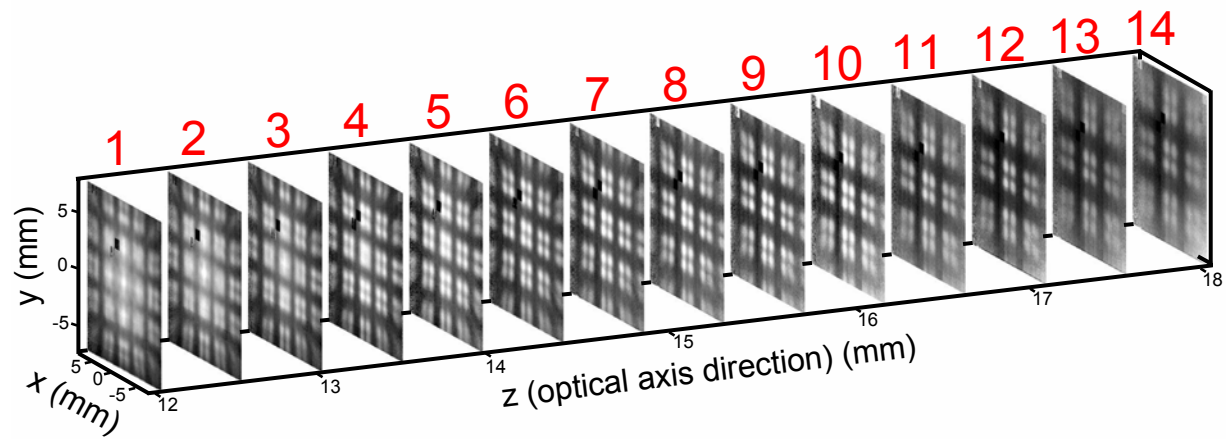
Supplementary Figure S18: The character “E” imaged by each pixel in the hemispherical camera when scanned over the entire projected image (scans from -40 to 40° in the θ and ϕ directions, 1.0° increments). The images cover varying portions of the hemispherical surface and are displayed as projected onto a planar surface.



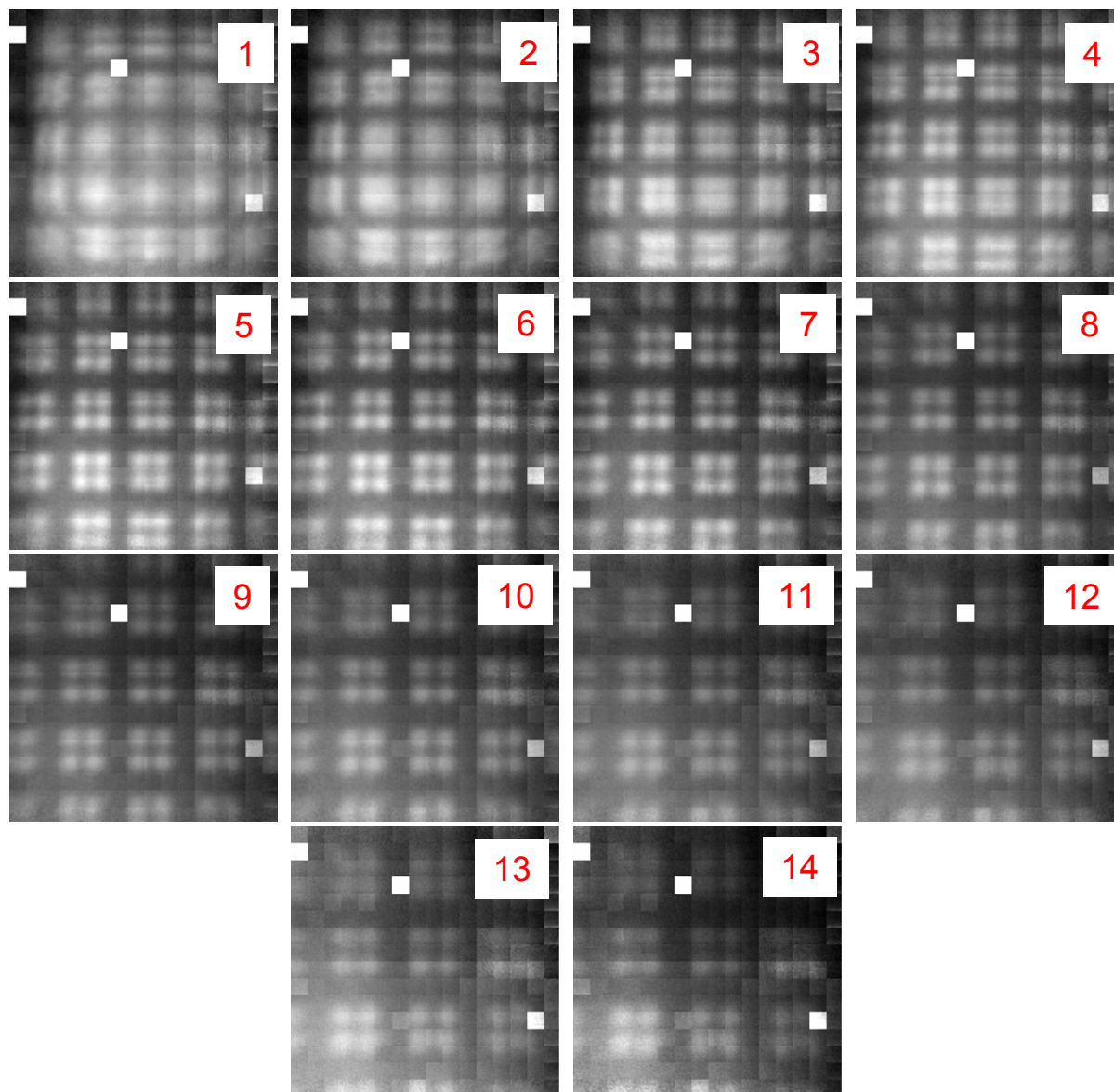
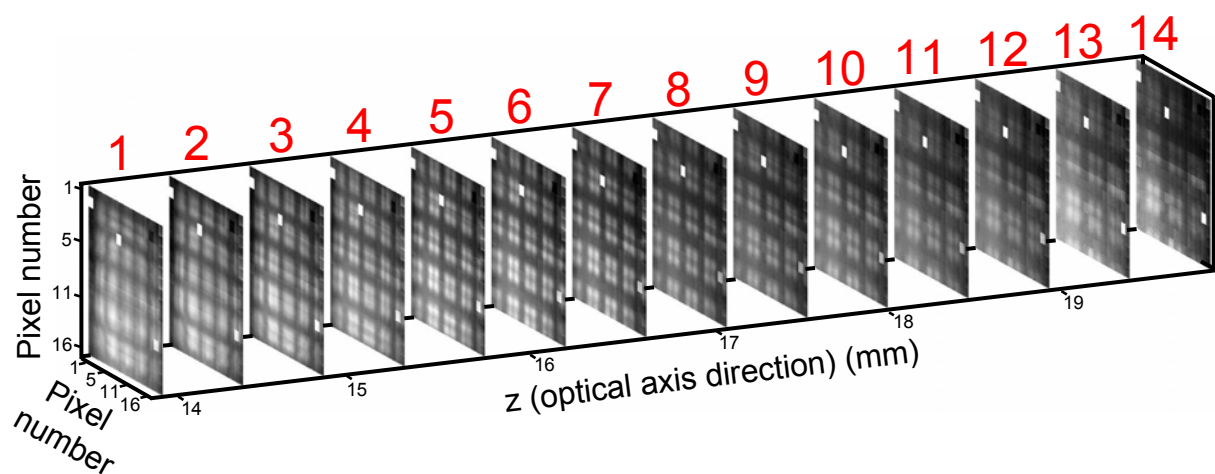
Supplementary Figure S19: A drawing of an eye imaged by each pixel in the hemispherical camera when scanned over the entire projected image (scans from -40 to 40° in the θ and ϕ directions, 0.5° increments). The images cover varying portions of the hemispherical surface and are displayed as projected onto a planar surface.



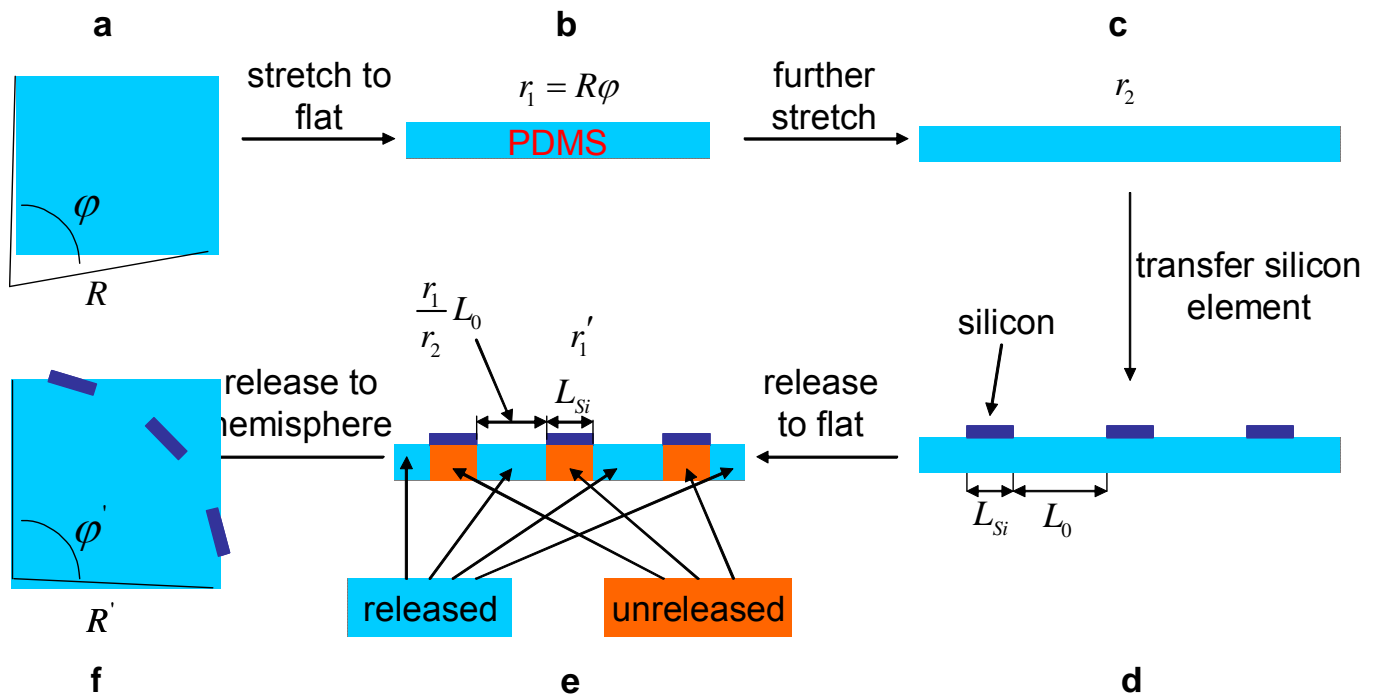
Supplementary Figure S20: High-resolution photographs on a planar screen positioned at varying distances from the lens. The images were acquired at distances between 12.15 (image #1, left) and 18.00 mm (image #13, right) from the lens and demonstrate the curvilinear nature of the optimal focal surface.



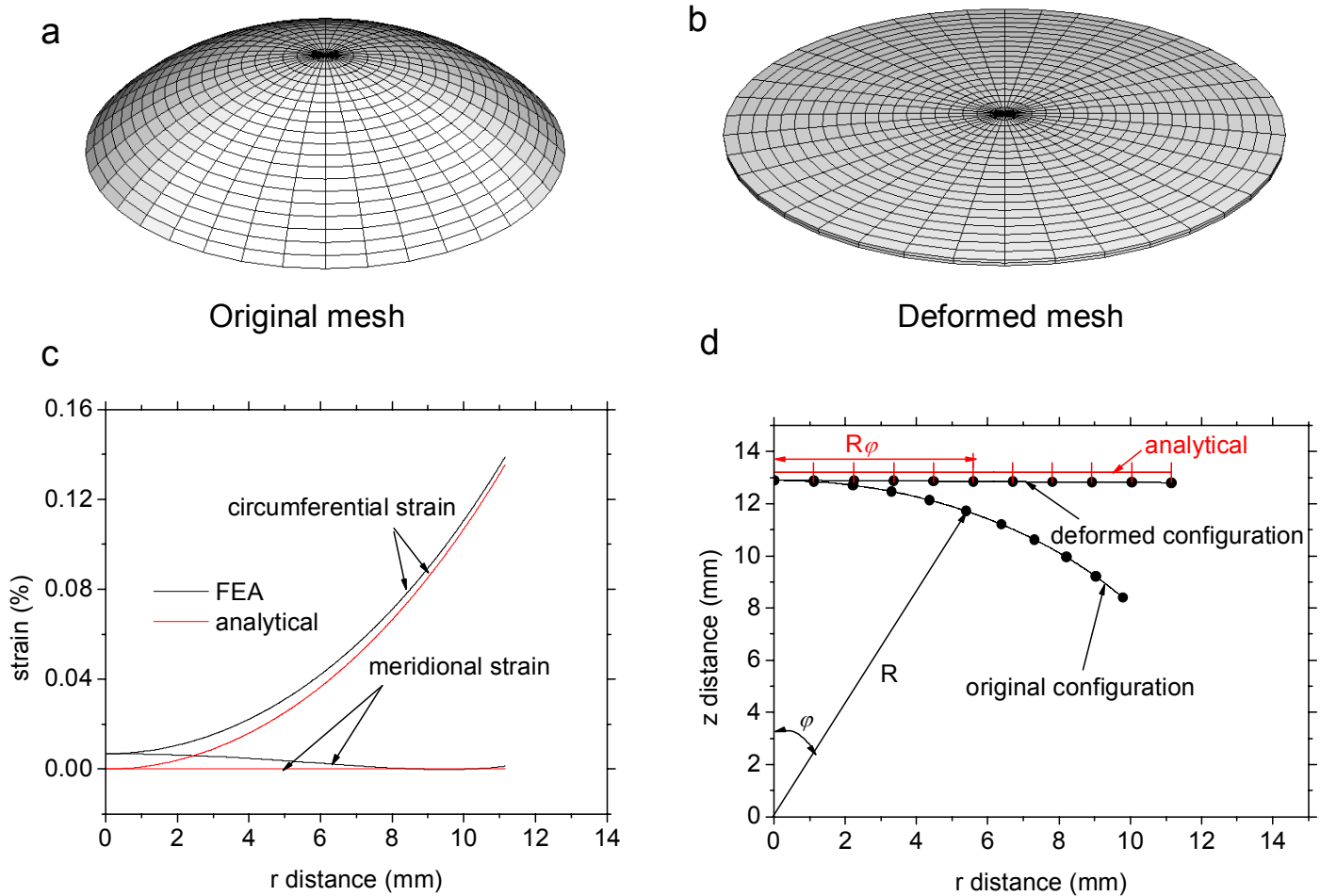
Supplementary Figure S21: Photographs acquired with the fabricated 16 by 16 planar camera at varying distances from the lens. The images were acquired at distances between 12.15 (image #1, left) and 18.00 mm (image #14, right) from the lens and demonstrate the curvilinear nature of the optimal focal surface.



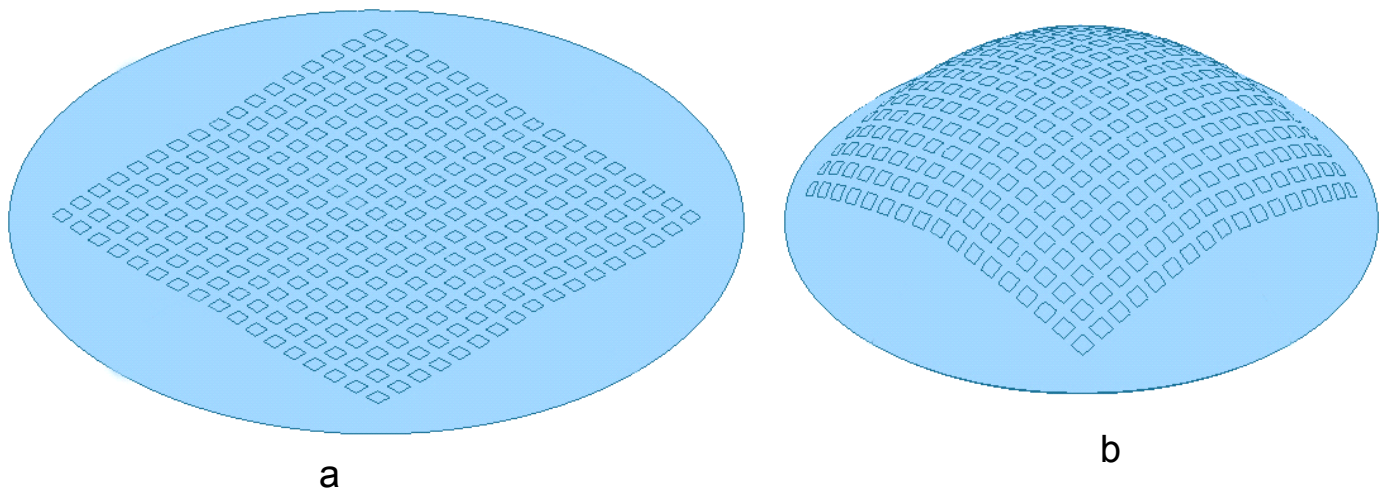
Supplementary Figure S22: Photographs acquired with the fabricated 16 by 16 hemispherical camera at varying distances from the lens. The images are plotted on planes as a function of pixel number. The images were acquired at distances between 13.95 (image #1, left) and 19.80 mm (image #14, right) from the lens.



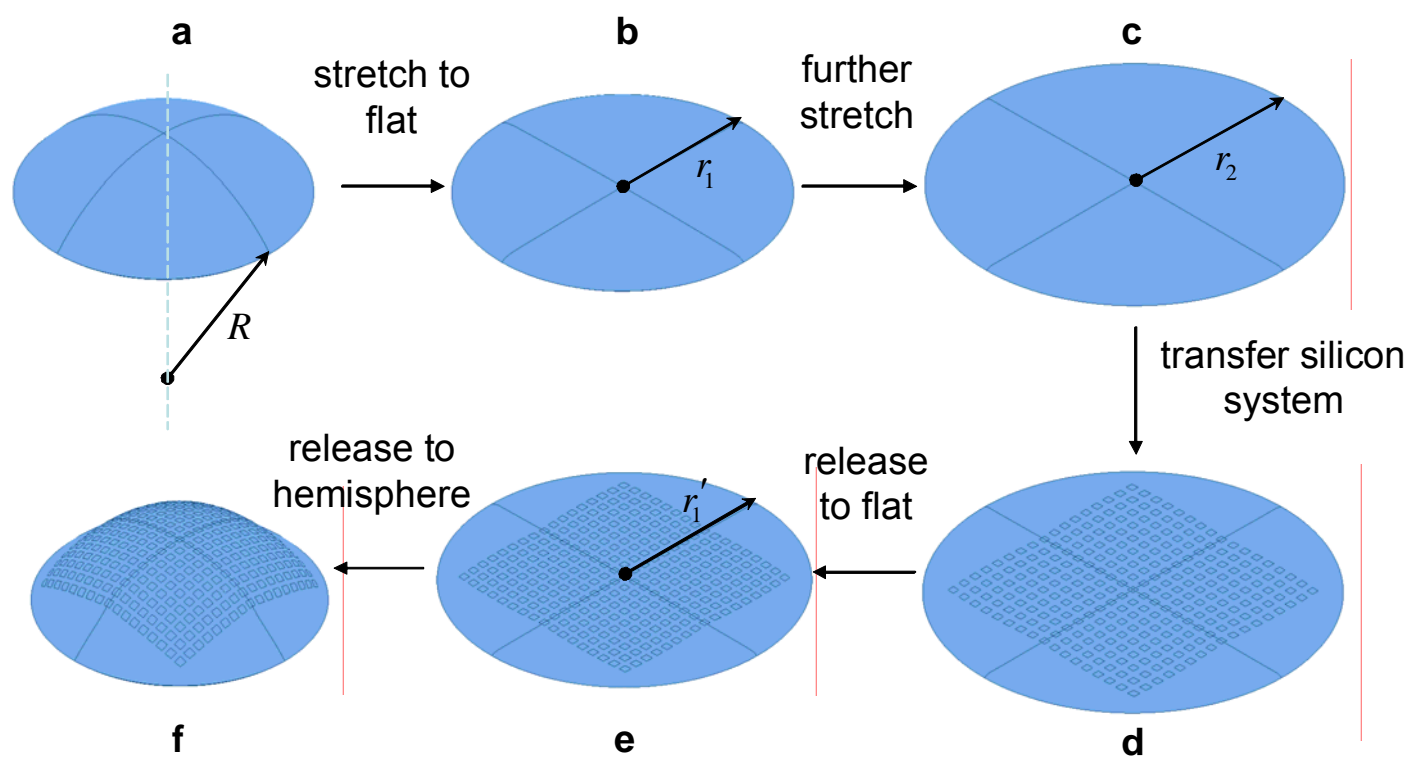
Supplementary Figure S23: Schematic illustration of the mapping of silicon elements onto a hemisphere. **a**, A PDMS hemispherical cap of radius R ; **b**, the cap is first stretched to an approximately flat plate of radius r_1 ; **c**, the flat plate is further stretched to a flat plate with radius r_2 ; **d**, the silicon elements are transferred onto the plate; **e**, the plate with Si elements is released to an approximately flat plate of radius r_1' ; **f**, further release leads to a new hemisphere of radius R' .



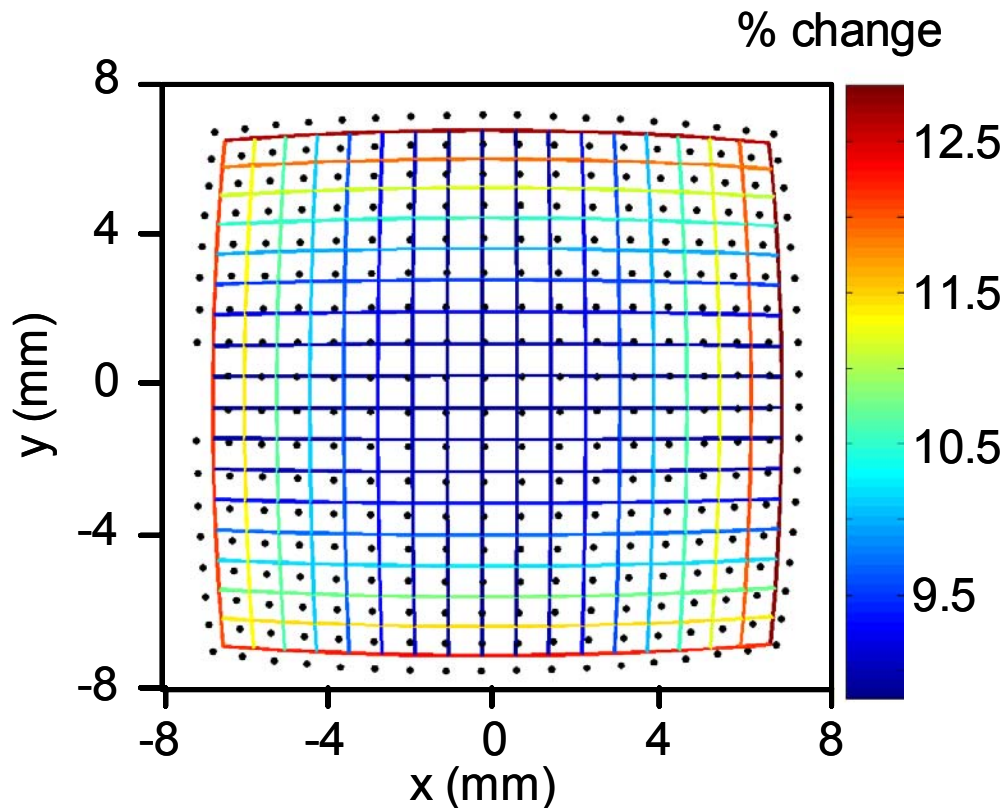
Supplementary Figure S24: Finite element analysis of the mapping from a hemisphere state to an approximately flat state. **a**, The original mesh for the PDMS hemispherical cap; **b**, the deformed mesh for the just flattened plate; **c**, the strain distribution in the flattened plate; and **d**, comparison of the mapping between finite element results and analytical solution.



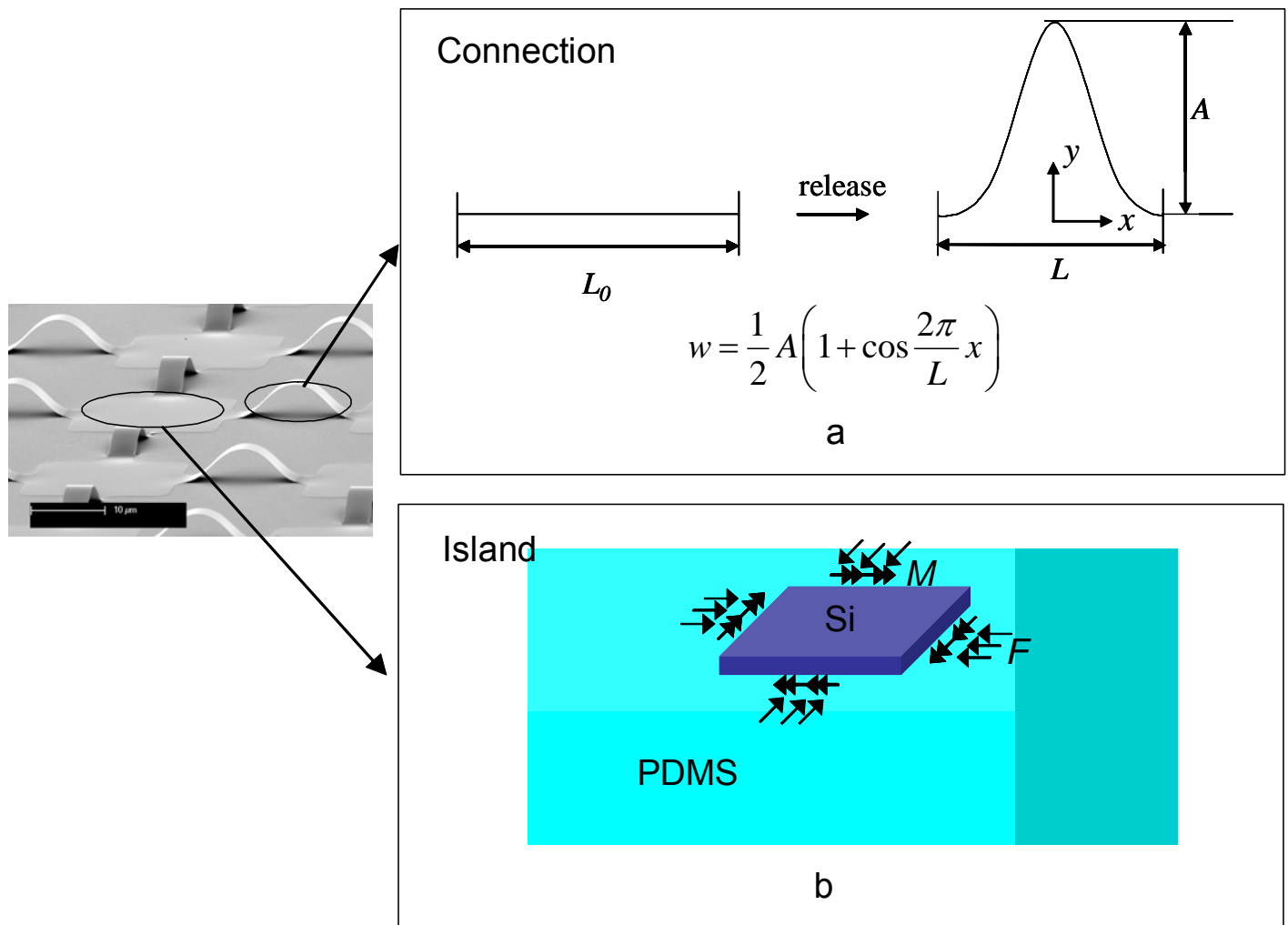
Supplementary Figure S25: The deformed shape of **a**, the flat, relaxed PDMS and silicon and **b**, the spherical, relaxed PDMS and silicon as calculated by finite element analysis.



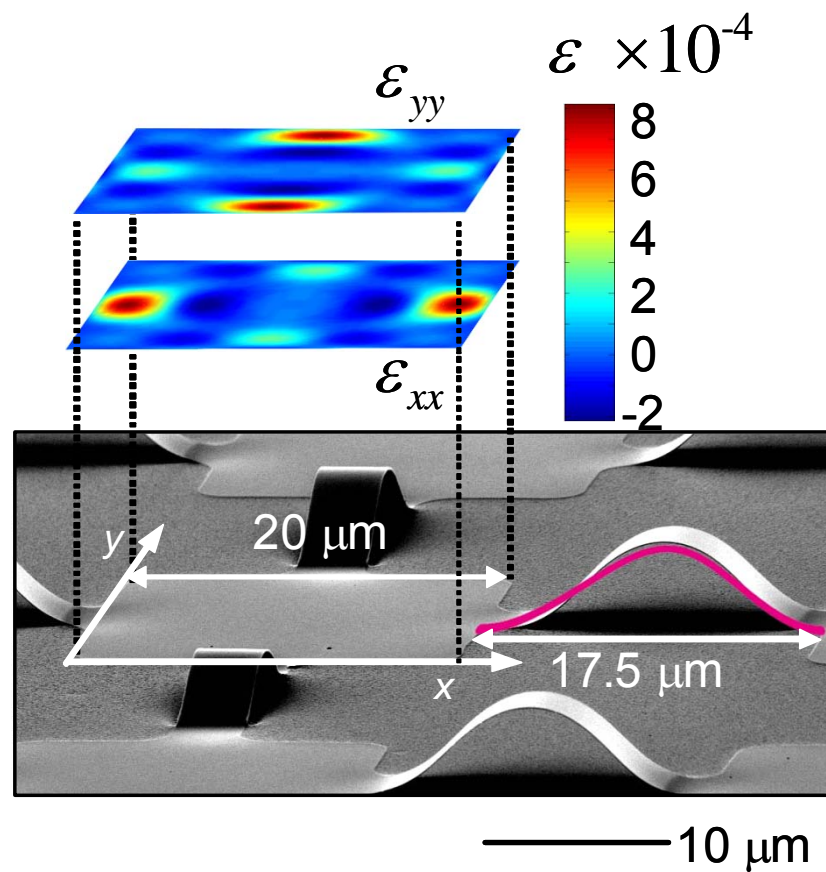
Supplementary Figure S26: Images of the mapping process as obtained by the finite element method.



Supplementary Figure S27: Experimentally measured map (black dots) of spatial positions of silicon elements (500x500 mm; 1.2 mm thick) across a 16 by 16 array on a hemispherical transfer element. The overlaid coloured mesh represents predictions for the planar to hemispherical transformation from the analytical mechanics model; the mesh nodes are the predicted spatial positions of the array and the segment colours indicate the percentage change of the distance between neighbouring elements across the array, compared to those designed in the planar configuration. The results indicate less than a ~3% variation, from minimum to maximum.



Supplementary Figure S28: Analytical model of **a**, the shape of the compressed connections and **b**, strain in the silicon elements.



Supplementary Figure S29: SEM highlighting a single pixel in a 16 by 16 array on a hemispherical detector, with theoretical results for the arc shapes and the distribution of strains, overlaid in colour.